arXiv:2603.06082v1 [cs.AI] 6 Mar 2026

Offline Materials Optimization with CliqueFlowmer

Jakub Grudzien Kuba[*] **Benjamin Kurt Miller**[†] **Sergey Levine**[*] **Pieter Abbeel**[*]

Abstract

Recent advances in deep learning inspired neural network-based approaches to *computational materials discovery* (CMD). A plethora of problems in this field involve finding materials that optimize a target property. Nevertheless, the increasingly popular generative modeling methods are ineffective at boldly exploring attractive regions of the materials space due to their maximum likelihood training. In this work, we offer an alternative CMD technique based on offline *model-based optimization* (MBO) that fuses direct optimization of a target material property into generation. To that end, we introduce a domain-specific model, dubbed *CliqueFlowmer*, that incorporates recent advances of clique-based MBO into transformer and flow generation. We validate CliqueFlowmer's optimization abilities and show that materials it produces strongly outperform those provided by generative baselines. To enable employment of CliqueFlowmer in specialized materials optimization problems and support interdisciplinary research, we open-source our code at

`https://github.com/znowu/CliqueFlowmer`.

1 Introduction

Large neural network models have recently enabled solving challenging artificial intelligence tasks such as language modeling, automated coding, and image generation (Achiam et al., 2023; Team et al., 2024; Ho et al., 2020; Esser et al., 2024). Meanwhile, scientific problems that deal with the world of atoms, rather than the world of bits, are yet to benefit from this revolution (Thiel, 2025). Indeed, exploration of new physical breakthroughs continues to take place in physical wet labs, and is driven by costly physical experimentation (Freese et al., 2024; Shahzad et al., 2024). One of such problems is *computational materials discovery* (CMD), wherein scientists strive to invent new chemical structures that display properties absent in known materials (Jain et al., 2013; Lin et al., 2025). A systematic, sample-efficient methodology for CMD has the potential to deliver structures that serve as catalysts for key energy-conversion reactions and as structural and functional components of advanced biomaterials. Such advances would greatly accelerate the development of clean-energy technologies and medical therapies, effectively extending the recent AI-driven progress from the world of bits to the world of atoms (Gokcekuyu et al., 2024; Han & Su, 2025).

Having realized the importance of this problem, AI researchers have been increasingly turning their attention to AI-driven CMD. Most commonly, the introduced methods have been utilizing the celebrated *diffusion* and *flow* models that had become very successful in the domain of image generation (Ho et al., 2020; Lipman et al., 2022; Miller et al., 2024; Inizan et al., 2025). While effective at harnessing the distribution of viable materials presented to them in the dataset, likelihood-based generative models do not actively explore the relation between the materials and their properties. This is a major impediment in settings where CMD is expected to optimize materials with respect to a specified metric (Yang et al., 2024; Havens et al., 2025). In the meantime, a new paradigm, known as *offline model-based optimization* (MBO) has made steps towards techniques that optimize *scientific*

[*]BAIR, UC Berkeley, Berkeley, California, USA. Corresponding author: `kuba@berkeley.edu`
[†]FAIR, Meta, San Francisco, California, USA

Preprint.

designs by bootstrapping models trained entirely on offline data (Kumar et al., 2021; Trabucco et al., 2022; Kuba et al., 2024). Nevertheless, MBO methods have been mainly deployed in standard benchmark tasks, free, for example, of the challenging intricacies of CMD in which data is inherently of the hybrid discrete-continuous nature, irregular shape, and subject to physical constraints.

To address the need for AI-driven CMD and the limitations of generative approaches, in this work, we introduce *CliqueFlowmer*—a model that renders material data tractable by MBO and enables optimizing material structures. The core of the model is an auto-encoder that converts the multi-modal, irregular material data into structured, finite-dimensional vectors that can be optimized with *clique-based* MBO (Kuba et al., 2024), and mapped back into the material form. These abilities are attained by a carefully engineered neural network architecture that utilizes transformers and combines them with generative learning techniques such as next-token prediction and flow matching, and MBO techniques such as clique decomposition (Grudzien et al., 2024). Empirically, utilizing data from Materials Project (Jain et al., 2013) as well as M3GNet (Chen & Ong, 2022) and MEGNet (Chen & Ong, 2022) as oracles for the studied properties, we show that materials optimized by CliqueFlowmer vastly outperform those sampled by generative baselines. Additionally, we hope that this work will attract attention to the field of MBO and will open up possibilities for more effective CMD methods.

2 Background

This section provides the necessary background on the key notions discussed by our work. First, we lay down foundations of material modeling that enables us to use machine learning methods in CMD. Then, we introduce the basic ideas of continuous normalizing flows (*i.e.,* flow matching). Lastly, we state the problem that we aim to solve (CMD) and formulate it through the lens of offline MBO.

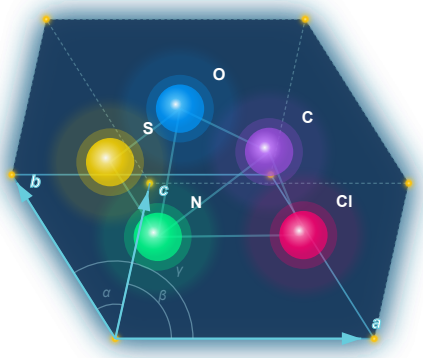

Figure 1: The unit cell of a hypothetical material. The cell has a shape of a parallelepiped determined by three axes, $\vec{a}$, $\vec{b}$, and $\vec{c}$. The angles between the axes are $\text{ang}(\vec{b}, \vec{c}) = \alpha$, $\text{ang}(\vec{c}, \vec{a}) = \beta$, $\text{ang}(\vec{a}, \vec{b}) = \gamma$. In this cell, there are five atoms, whose type sequence is $\mathbf{a} = [\text{N, Cl, C, O, S}]$.

2.1 Modeling Materials

We characterize a material M by its *unit cell*—the material's unit amount. The cell has a shape of a parallelepiped determined by the lengths of its axes, $(a, b, c) \in \mathbb{R}^3_+$, and angles between them, $(\alpha, \beta, \gamma) \in (0, \pi)^3$. The content of the cell is a set of N_{atom} (which varies between materials) atoms that is represented by the sequence $\mathbf{a} \in \mathcal{A}^{N_{\text{atom}}}$ of their types, as well as their positions $\mathbf{X} \in [0, 1)^{N_{\text{atom}} \times 3}$ expressed in the basis induced by (a, b, c) and (α, β, γ). Thus, the space of materials M can be embedded in the product $\mathcal{M} = \mathbb{R}^3_+ \times (0, \pi)^3 \times (\mathcal{A} \times [0, 1)^3)^*$, and a single material can be characterized as a tuple $[(a, b, c), (\alpha, \beta, \gamma), \mathbf{a}, \mathbf{X}]$. [3] In this paper, we denote the geometrical part of the material as $\mathbf{G} = [(a, b, c), (\alpha, \beta, \gamma), \mathbf{X}]$, and thus can write $[\mathbf{a}, \mathbf{G}]$ to represent material M.

2.2 Flow Matching

The goal of a continuous normalizing flow (Lipman et al., 2022) is to learn sampling from a data distribution $p_{\text{data}}(\mathbf{x})$. To that end, one sets the target distribution $p_1(\mathbf{x}) = p_{\text{data}}(\mathbf{x})$, as well as *source* distribution $p_0(\mathbf{x}) = p_{\text{source}}(\mathbf{x})$, such as the standard-normal. To learn to turn a sample from $p_{\text{source}}(\mathbf{x})$ into one from $p_{\text{data}}(\mathbf{x})$, one interpolates noise and data,

$$\mathbf{x}_t = (1 - t) \cdot \mathbf{x}_0 + t \cdot \mathbf{x}_1, \quad \text{where} \quad \mathbf{x}_0 \sim p_0(\mathbf{x}),\ \mathbf{x}_1 \sim p_1(\mathbf{x})\ \ \&\ \ t \sim p_{\text{time}}(t),$$

and passes the mixture, together with timestep information, to a *velocity* neural network that minimizes

$$\mathbb{E}_{\mathbf{x}_0 \sim p_0, \mathbf{x}_1 \sim p_1, t \sim p_{\text{time}}} \left[\left(v_\theta(\mathbf{x}_t, t) - (\mathbf{x}_1 - \mathbf{x}_0) \right)^2 \right].$$

[3] $\mathcal{S}^*$ denotes the countable union of the products of the set $\mathcal{S}$ with itself. That is, $\mathcal{S}^* = \cup_{n=1}^{\infty} \mathcal{S}^n$.

Once learned, the velocity network can be used to sample from the target distribution by solving the following ordinary differential equation (ODE) with initial conditions,

$$\mathrm{d}\mathbf{x}_t = v_\theta(\mathbf{x}_t, t)\mathrm{d}t, \quad \mathbf{x}_0 \sim p_0(\mathbf{x}),$$

from $t = 0$ to $t = 1$, which results in a sample $\mathbf{x}_1 \sim p_1(\mathbf{x})$. Typically, the ODE is solved numerically, by discretizing the time interval $[0, 1]$ into N_{step} steps and using, *e.g.,* the Euler method. In this paper, we will use continuous normalizing flows to model the geometry of materials.

2.3 Model-Based Optimization in Computational Materials Discovery

We consider a function $f(\mathsf{M}) \in \mathbb{R}$, often referred to as *target property*, and assume that we are given a finite dataset $\mathcal{D} = \{\mathsf{M}^i, \mathrm{y}^i = f(\mathsf{M}^i)\}_{i=1}^N$ of examples of materials and their values of the property. Given this dataset, our goal is to discover materials that optimize the property,

$$\min_{\mathsf{M} \in \mathcal{M}} f(\mathsf{M}) \tag{1}$$

without the necessity to evaluate consecutive candidates in a wet lab[4]. That is, we want to do this *fully offline*. The standard approach to this problem consists of two steps: *1)* learning to sample new materials with a generative model $p_\theta(\mathsf{M})$, and *2)* to select the most promising candidate out of N_{prop} proposed materials (Chen & Gu, 2020; Park et al., 2024; Zeni et al., 2025). However, this approach is quite inefficient as an optimization algorithm, since sampling from $p_\theta(\mathsf{M})$ only explores the regions of the materials space that have been seen during training of the model. Thus, new methods that explore attractive regions of the materials space more effectively are desirable (more background in Appendix A).

In this work, we suggest to solve the optimization problem in Equation (1) directly. That is, we will use tools from offline *model-based optimization* (MBO) to model the target property $f(\mathsf{M})$ and find candidates for its minimizers. To enable application of these techniques in computational materials discovery (CMD), for the first time, we introduce a novel neural-network model, dubbed *CliqueFlowmer*, that turns materials into variables tractable by MBO.

3 CliqueFlowmer

This section introduces the architecture and the training algorithm of our MBO model for CMD. It consists of a few components. In Section 3.1 we introduce an encoder that maps a material M to a continuous latent representation $\mathbf{z}$. Then, Section 3.2 describes a decomposable model that predicts the property of interest from $\mathbf{z}$. Section 3.3 delineates a decoder that reconstructs the material—both the atom types and the geometry, from the representation. As we demonstrate later, such a setup allows to parameterize materials as continuous vectors which can be optimized for properties with gradient-based techniques (see Figure (2)).

3.1 Encoder

Our encoder has to combine four distinct pieces of information: lattice lengths (a, b, c), lattice angles (α, β, γ), atom positions $\mathbf{X}$, and atom types $\mathbf{a}$ (the latter two being irregular), and produce a fixed-dimensional continuous vector $\mathbf{z} \in \mathbb{R}^{d_{\mathbf{z}}}$. To do it, first, we map the continuous inputs to vectors of size d_{model} with their corresponding MLPs,

$$\mathbf{h}^{\text{len}} = \mathrm{MLP}_\theta^{\text{len}}(a, b, c), \quad \mathbf{h}^{\text{ang}} = \mathrm{MLP}_\theta^{\text{ang}}(\alpha, \beta, \gamma), \quad \mathbf{H}^{\text{pos}} = \mathrm{MLP}_\theta^{\text{pos}}(\mathbf{X})$$

and we map the atom types to continuous d_{model}-dimensional embeddings $\mathbf{H}^{\text{atom}}$. The MLP-produced hidden states are then concatenated, $\mathbf{H}^{\text{in}} = [\mathbf{h}^{\text{len}}, \mathbf{h}^{\text{ang}}, \mathbf{H}^{\text{pos}}]$, and passed into a transformer, where they are conditioned by $\mathbf{H}^{\text{atom}}$ via adaptive layer-norm (Peebles & Xie, 2023, AdaLN) that replaces layer-norm (Lei Ba et al., 2016) from the standard transformer (Vaswani et al., 2017),

$$\mathbf{H}^{\text{out}} = T_\theta^{\text{enc}}(\mathbf{H}^{\text{in}}, \mathbf{H}^{\text{atom}}).$$

For a single instance of N_{atom} atoms in the unit cell, the output of the transformer is a tensor of shape $(2 + N_{\text{atom}}) \times d_{\text{model}}$, thus depending on the cell size. To produce a fixed-dimensional representation $\mathbf{z}$,

[4]Maximization problems can be represented analogously and solved using the same techniques.

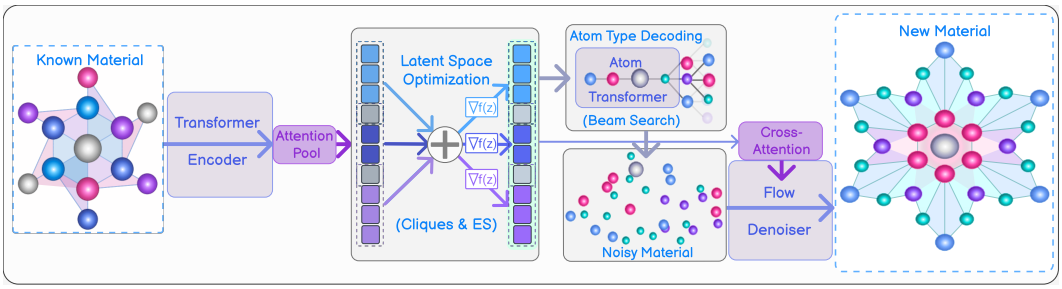

Figure 2: Computational materials discovery through MBO with CliqueFlowmer. Known materials are encoded, with a transformer encoder and an attention-based pooling layer, into a fixed-dimensional latent space. The latent variable admits a clique decomposition, with respect to the target property, where each clique contributes additively to the target property. The representations are optimized, with evolution strategies-based gradient optimization. Atom types are then decoded with an autoregressive transformer and beam search. The flow model reconstructs the material's geometry from the atom sequence and the latent representation by which it is conditioned via cross-attention.

we pool the tensor along the first dimension, using attention with a learnable query vector $\mathbf{q} \in \mathbb{R}^{d_{\text{model}}}$, yielding a hidden state,

$$\mathbf{h}^{\text{pool}} = \text{Att}(\mathbf{q}, \mathbf{K}\mathbf{H}^{\text{out}}, \mathbf{V}\mathbf{H}^{\text{out}}) \in \mathbb{R}^{d_{\text{model}}}, \tag{2}$$

which is further post-processed by GELU (Hendrycks & Gimpel, 2016) and layer-norm, yielding $\mathbf{h}^{\text{post}}$. It is then fed to a linear layer that produces the mean and log-standard deviation parameters of the normal distribution of the latent representation,

$$[\mu_{\mathbf{z}},\ \log \sigma_{\mathbf{z}}] = \text{Lin}_\theta(\mathbf{h}^{\text{post}}), \quad \mathbf{z} \sim \mathcal{N}(\mu_{\mathbf{z}}, \sigma_{\mathbf{z}}^2).$$

We highlight that the pooling layer from Equation (2) is what enables us to navigate the transdimensional materials space $\mathcal{M}$ with a fixed-dimensional vector space, paving the road for MBO.

3.2 Predictor

Once sampled, in addition to the standard flat form, the latent vector attains a form of a chain of cliques $\texttt{chain}(\mathbf{z}, d_{\text{clique}}, d_{\text{knot}})$ of clique size d_{clique} and knot size d_{knot}. That is, it is a $N_{\text{clique}} \times d_{\text{clique}}$ matrix $\mathbf{Z}$ with entry values from $\mathbf{z}$ such that $\mathbf{Z}_{i,j} = \mathbf{z}_k$, where $k = (i-1) \cdot (d_{\text{clique}} - d_{\text{knot}}) + j$, *i.e.*, the last d_{knot} entries of row i and the first d_{knot} entries of row $i+1$, for $i = 1, \ldots, N_{\text{clique}} - 1$, are equal. We write $\mathbf{Z}_i$ to denote its ith row. The matrix is then fed to an MLP predictor of property $\mathbf{y} = f(\mathsf{M})$ that decomposes its prediction over the cliques of $\mathbf{Z}$,

$$f(\mathsf{M}) \approx f_\theta(\mathbf{z}) = \sum_{c=1}^{N_{\text{cliques}}} f_\theta(\mathbf{Z}_c, c).$$

Imposing such a decomposable structure on the latent space is known to improve the effectiveness of MBO (Kuba et al., 2024). Intuitively (see Figure 2), it enables composing optimal in-distribution examples of each clique to form a competitive in-distribution solution—a property also known as *stitching* (Fu et al., 2020; Shin et al., 2025).

3.3 Decoder

The decoder consists of two modules: the atom type decoder and the geometry decoder. The former infers the atom types given the latent representation, $p_\theta(\mathbf{a}|\mathbf{z})$, and the latter infers the unit cell geometry given the latent representation and the atom types, $p_\theta(\mathbf{G}|\mathbf{z}, \mathbf{a})$.

Atom types. The atom type decoder is quite straightforward—we utilize the standard causal transformer with next-token prediction which we condition on the latent representation via AdaLN. To that end, first, we map the $d_{\mathbf{z}}$-dimensional $\mathbf{z}$ to the d_{model}-dimensional space as

$$\mathbf{z}^{\text{mod}} = \text{LayerNorm}(\text{GELU}(\text{Lin}_\theta(\mathbf{z}))), \tag{3}$$

and then use it in combination with adaptive layer-norm inside of the causal transformer to produce a hidden state

$$\mathbf{h}_{k+1} = T_\theta^{\text{dec}}(\mathbf{a}_{0:k}, \mathbf{z}^{\text{mod}})_{k+1},$$

for $k = 0, \ldots, N_{\text{atom}}$, where a_0 and $\mathrm{a}_{N_{\text{atom}}+1}$ are $\langle\text{Start}\rangle$ and $\langle\text{Stop}\rangle$ tokens, respectively. That hidden state is then refined into log-likelihoods with an MLP and a log-softmax layer that predicts the next (atom type) token.

Geometry. We decode the shape of the unit cell and the atom positions with a continuous normalizing flow, conditioned on $\mathbf{z}$, for which we build another specialized transformer. We use the flow-matching framework, wherein we decode the material geometry $\mathbf{G} = [(a, b, c),\ (\alpha, \beta, \gamma),\ \mathbf{X}]$ by, first, initializing at a sample from a prior distribution and, then, solving an ODE,

$$\text{Sample} \quad \mathbf{G}_0 = [(a, b, c),\ (\alpha, \beta, \gamma),\ \mathbf{X}]_0 \sim p_0(\mathbf{G}|\mathbf{a}), \quad \text{Solve} \quad \mathrm{d}\mathbf{G}_t = V_\theta(\mathbf{G}_t, t|\mathbf{a}, \mathbf{z})\mathrm{d}t,$$

from $t = 0$ to $t = 1$, where $V_\theta(\mathbf{G}_t, t|\mathbf{a}, \mathbf{z})$ is a transformer denoiser. The prior distribution $p_0(\mathbf{G}|\mathbf{a}) = p_0^{\text{len}}(a, b, c|\mathbf{a}) \cdot p_0^{\text{ang}}(\alpha, \beta, \gamma|\mathbf{a}) \cdot p_0^{\text{pos}}(\mathbf{X}|\mathbf{a})$ is modeled meticulously—first, angles are modeled as random uniform in interval $(\pi/3, 2\pi/3)$, and positions are random uniform on $(0, 1)$. The prior over the lengths is chosen so that the density of the unit cell $N_{\text{atom}}/\text{Vol}(\mathsf{M})$ is invariant of the number of atoms, similarly to Zeni et al. (2023). To that end, we observe that $\text{Vol}(\mathsf{M}) \propto abc$ and, thus, we compose sampling the lengths from an independent prior, $(\underline{a}, \underline{b}, \underline{c}) \sim \underline{p}^{\text{len}}(\underline{a}, \underline{b}, \underline{c})$, with scaling by $\sqrt[3]{N_{\text{atom}}}$. Lastly, the prior $\underline{p}^{\text{len}}(\underline{a}, \underline{b}, \underline{c})$ over N_{atom} independent lengths is modeled as a log-normal distribution whose parameters are estimated from training data (more details in Appendix E).

Similarly to the encoder, given a noisy unit cell shape and atom positions $\mathbf{G}_t = [(a, b, c), (\alpha, \beta, \gamma), \mathbf{X}]_t$ at time t, we embed them in the d_{model}-dimensional space with MLPs. This is then fed to a (non-causal) transformer that is conditioned on the embeddings of the decoded atom types $\mathbf{H}^{\text{atom}}$ via AdaLN. Crucially, each block of the transformer contains a cross-attention layer between the hidden states and the latent representations in form $\mathbf{Z} = \texttt{chain}(\mathbf{z}, d_{\text{clique}}, d_{\text{knot}})$. More specifically, cliques of $\mathbf{Z}$ get first mapped to the d_{model}-dimensional space

$$\mathbf{H}^{\mathbf{z}} = \text{LayerNorm}(\text{GELU}(\text{MLP}_\theta^{\text{lat}}(\mathbf{Z}))),$$

and a cross-attention layer is added between the self-attention and feed-forward layers of the transformer block

$$\mathbf{H}_t^{\text{cross}} = \mathbf{H}_t^{\text{self}} + \text{CrossAtt}(\mathbf{H}_t^{\text{self}}, \mathbf{H}^{\mathbf{z}})$$

(more information in Appendix D). The output hidden state $\mathbf{O}_t$ of the transformer is then decomposed into the lengths, angles, and position parts, and each of them is used to predict the corresponding modality with an MLP,

$$\hat{\mathbf{v}}_t^{\text{len}} = \text{MLP}_\theta^{\text{len}}(\mathbf{o}_t^{\text{len}}), \quad \hat{\mathbf{v}}_t^{\text{ang}} = \text{MLP}_\theta^{\text{ang}}(\mathbf{o}_t^{\text{ang}}), \quad \hat{\mathbf{V}}_t^{\text{pos}} = \text{MLP}_\theta^{\text{pos}}(\mathbf{O}_t^{\text{pos}})$$

which together form the prediction from our denoiser, $V_\theta(\mathbf{G}_t, t|\mathbf{a}, \mathbf{z}) = [\hat{\mathbf{v}}_t^{\text{len}}, \hat{\mathbf{v}}_t^{\text{ang}}, \hat{\mathbf{V}}_t^{\text{pos}}]$. Lastly, to sample the denoising timestep for training, we draw a sample from, our novel, *lifted logit-normal* distribution, which is a Bernoulli mixture of the logit-normal distribution and the uniform distribution (consult Appendix H for more information).

3.4 Training

The goal of training CliqueFlowmer is to learn a map $p_\theta(\mathbf{z}|\mathbf{a}, \mathbf{G})$ of a material $\mathsf{M} = [\mathbf{a}, \mathbf{G}]$ to a fixed-dimensional continuous vector $\mathbf{z}$, a decomposable approximator $f_\theta(\mathbf{z})$ of the target property, and the inverse $p_\theta(\mathbf{a}, \mathbf{G}|\mathbf{z}) = p_\theta(\mathbf{a}|\mathbf{z})p_\theta(\mathbf{G}|\mathbf{a}, \mathbf{z})$ of the encoding map. Thus, to train CliqueFlowmer, we must combine training of its four integrated submodules. At the nucleus of this fusion there is sampling the latent representation $\mathbf{z} \sim p_\theta(\mathbf{z}|\mathbf{a}, \mathbf{G})$—given this vector, the atom type decoder learns to maximize the conditional next-token log-likelihood

$$-\mathcal{L}_{\text{atom}}(\mathbf{a}, \mathbf{z}) = \sum_{i=0}^{N_{\text{atom}}} \log p_\theta(\mathrm{a}_{i+1}|\mathbf{a}_{0:i}, \mathbf{z}),$$

where $\mathrm{a}_0 = \langle\text{Start}\rangle$ and $\mathrm{a}_{N_{\text{atom}}+1} = \langle\text{Stop}\rangle$ are *Start* and *Stop* tokens.

Meanwhile, the flow-matching model that uses cross-attention to condition on the clique form $\mathbf{Z}$ of the latent, samples a noise geometry $\mathbf{G}_0$ for a cell with N_{atom} atoms, interpolates it with the ground-truth geometry at a random timestep, $\mathbf{G}_t = (1-t)\cdot\mathbf{G}_0 + t\cdot\mathbf{G}$, and minimizes the difference between the velocity network's prediction and the path between geometries,

$$\mathcal{L}_{\text{len}}(\mathbf{a},\mathbf{z},\mathbf{G},\mathbf{G}_0) = \big((a-a_0, b-b_0, c-c_0) - \hat{\mathbf{v}}_t^{\text{len}}\big)^2$$
$$\mathcal{L}_{\text{ang}}(\mathbf{a},\mathbf{z},\mathbf{G},\mathbf{G}_0) = \big((\alpha-\alpha_0, \beta-\beta_0, \gamma-\gamma_0) - \hat{\mathbf{v}}_t^{\text{ang}}\big)^2$$
$$\mathcal{L}_{\text{pos}}(\mathbf{a},\mathbf{z},\mathbf{G},\mathbf{G}_0) = \sum_{i=1}^{N_{\text{atom}}} \big((\mathbf{x}^i - \mathbf{x}_0^i) - \hat{\mathbf{v}}_t^{\text{pos},i}\big)^2.$$

While training the flow denoiser, we mask the latent $\mathbf{z}$ and replace it with a random normal noise, $\epsilon_{\mathbf{z}} \sim \mathcal{N}(\mathbf{0}_{d_{\mathbf{z}}}, \mathbf{I}_{d_{\mathbf{z}}})$ with probability $p_{\text{lat}} = 0.1$. We decompose the flow loss into distinct components to ensure that the unit cell (lengths and angles) receives equal weight for every material in the batch. For clarity, we define the sum of flow losses as

$$\mathcal{L}_{\text{flow}}(\mathbf{a},\mathbf{z},\mathbf{G},\mathbf{G}_0) = \mathcal{L}_{\text{len}}(\mathbf{a},\mathbf{z},\mathbf{G},\mathbf{G}_0) + \mathcal{L}_{\text{ang}}(\mathbf{a},\mathbf{z},\mathbf{G},\mathbf{G}_0) + \tau_{\text{pos}}\cdot\mathcal{L}_{\text{pos}}(\mathbf{a},\mathbf{z},\mathbf{G},\mathbf{G}_0),$$

where τ_{pos} is a positive scalar. Further, the latent representation, in its clique form, is also tasked with minimizing the prediction error of the target property,

$$\mathcal{L}_{\text{pred}}(\mathsf{M},\mathbf{z}) = \big(f_\theta(\mathbf{z}) - f(\mathsf{M})\big)^2,$$

and the clique-based KL-divergence is computed for the parameters of the normal distribution of $\mathbf{z}$,

$$\mathcal{L}_{\text{lat}}(\mathsf{M},\mu_{\mathbf{z}},\sigma_{\mathbf{z}}) = \text{KL}\big(\mathcal{N}(\mu_{\mathbf{z},c}, \sigma^2_{\mathbf{z},c}),\ \mathcal{N}(\mathbf{0}_{d_{\text{clique}}}, \mathbf{I}_{d_{\text{clique}}})\big), \tag{4}$$

where the clique c is drawn from the uniform distribution $U[N_{\text{clique}}]$ (Kuba et al., 2024). Summarizing, and writing $\mathsf{M} = [\mathbf{a}, \mathbf{G}]$ where possible, the total expected loss is

$$\mathcal{L}(\theta) = \mathbb{E}_{\mathsf{M}\sim\mathcal{D},\mathbf{z}\sim p_\theta,\mathbf{G}_0\sim p_0}\big[\mathcal{L}_{\text{atom}}(\mathbf{a},\mathbf{z}) + \mathcal{L}_{\text{flow}}(\mathsf{M},\mathbf{z},\mathbf{G}_0) + \tau_{\text{pred}}\mathcal{L}_{\text{pred}}(\mathsf{M},\mathbf{z}) + \beta\mathcal{L}_{\text{lat}}(\mathsf{M},\mu_{\mathbf{z}},\sigma_{\mathbf{z}})\big],$$

where β and τ_{pred} are positive scalars which we warm up linearly one after another.

3.5 Computational Materials Discovery with CliqueFlowmer

To optimize new materials with our model, we conduct a form of gradient-based search in the representation space. We initialize this process by encoding a sample of existing materials with the encoder, $\mathbf{z} = \text{Enc}_\theta(\mathbf{a},\mathbf{G})$. Then, we optimize the prediction of the target property,

$$\mathbf{z}_\star = \underset{\mathbf{z}^{\text{new}}}{\arg\min}\, f_\theta(\mathbf{z}^{\text{new}}). \tag{5}$$

The choice of the minimization algorithm plays a significant role. While we have found that exact back-propagation of Equation (5) is prone to adversarial exploitation of the model, back-propagation-free evolution strategies (Salimans et al., 2017, ES) was very effective (see Section 4.2). That is, at every iteration, we draw N_{pert} noise vectors ϵ from the standard normal distribution, $\epsilon \sim \mathcal{N}(\mathbf{0}_{d_{\mathbf{z}}}, \mathbf{I}_{d_{\mathbf{z}}})$, and compute the predicted values $f_\theta(\mathbf{z} + \sigma\epsilon)$ of the perturbations of $\mathbf{z}$ at scale σ. Then, we rank these perturbations, $\epsilon^1, \ldots, \epsilon^{N_{\text{pert}}}$, based on the predicted values of f (so that the smallest value gets the lowest rank). We standardize the ranks to have zero mean and unit variance, $i \mapsto R^i$, for $i = 1, \ldots, N_{\text{pert}}$, and compute the ES gradient as

$$\hat{\nabla}^{\text{ES}}(\mathbf{z}) = \frac{1}{N_{\text{pert}}\sigma}\sum_{i=1}^{N_{\text{pert}}} R^i\epsilon^i. \tag{6}$$

Additionally, we use antithetic sampling (see Appendix B for more information about ES). Then, we take a gradient step with AdamW optimizer (Loshchilov et al., 2017). The weight decay step of the optimizer, $\mathbf{z} \mapsto (1-\lambda)\mathbf{z}$, is crucial since it brings the optimized latent variable closer to the origin. In effect, this step increases the likelihood of the latent under the Gaussian prior that CliqueFlowmer was trained with (see Equation (4)), which mitigates the problem of going out of distribution with $\mathbf{z}$.

Given an optimized latent representation $\mathbf{z}_\star$, we modulate it with Equation (3), and pass to the atom-type decoder, from which we sample the atom-type sequence using beam search (see Appendix A) with beam width $N_{\text{beam}} = 10$,

$$\mathbf{a}_\star \sim \text{BeamSearch}(T_\theta^{\text{dec}}, \mathbf{z}_\star^{\text{mod}}).$$

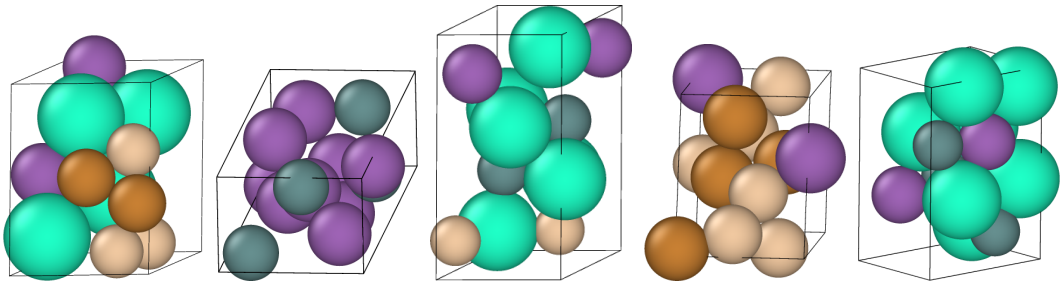

(a) Dy_3CuSi_2Sb (b) Cu_2Si_3Sb (c) $Dy_3SiGeSb$ (d) Cu_2Si_3Sb (e) $Dy_7(Ge_2Sb)_2$

Figure 3: Examples of materials optimized by CliqueFlowmer for band gap minimization. Each figure shows a material's unit cell, and the caption describes its composition. We can observe that the optimized materials often include Dysprosium (Dy) and Silicon (Si) as components. The corresponding band gap values are 0.06, 0.01, 0.14, 0.02, and 0.03.

Next, we consider the clique form of the latent representation, $\mathbf{Z}_\star = \texttt{chain}(\mathbf{z}_\star, d_{\text{clique}}, d_{\text{knot}})$, and pass it to our continuous normalizing flow model, from which we decode the material geometry. For this end, we use the *Euler method* with *classifier-free guidance* (Ho & Salimans, 2022, CFG), in which the effective velocity used in the ODE is

$$V_\theta^\omega(\mathbf{G}_t, t, \mathbf{z}_\star) = (1+\omega) \cdot V_\theta(\mathbf{G}_t, t, \mathbf{z}_\star) - \omega \cdot V_\theta(\mathbf{G}_t, t, \epsilon_{\mathbf{z}}),$$

where $\epsilon_{\mathbf{z}}$ is standard normal noise. In our experiments, we used $\omega = 2$ (see Appendix C for ablations). We provide a discussion on the time complexity of this procedure in Appendix I.

4 Experiments

We tested CliqueFlowmer in two tasks for which we trained two separate models. Both of them were trained on the MP-20 dataset, with the standard 60-20-20% train-val-test split, that contains 45K example materials in total (Xie et al., 2021) for a total of 7×10^5 gradient steps with batch size of 1024. In the first task, for the role of the target property, we chose the predicted formation energy per atom from M3GNet (Chen & Ong, 2022), and for the second one, the band gap predicted by MEGNet (Chen et al., 2019),

$$f(\mathsf{M}) = \frac{E_{\text{form}}(\mathsf{M})}{N_{\text{atom}}} \quad \text{(Formation Energy)}, \qquad f(\mathsf{M}) = \Delta_{\text{band}}(\mathsf{M}) \quad \text{(Band Gap)}.$$

It is worth noting that, for materials scientists, formation energy is not the most useful property to minimize since it doesn't translate to any extravagant physical behavior. Nevertheless, formation energy oracles, such as M3GNet, are easily accessible and accurate (in fact more accurate than band gap oracles), and thus suffice to demonstrate the capability of our method. Note also that these target properties, coming from ML oracles, introduce a synthetic bias into our model's training. While this may weaken the physical relevance of materials we discover, optimization of these properties provides a valid test for MBO methods in the CMD space. In the following subsections, we evaluate CliqueFlowmer for such abilities and investigate the material representations it learned.

4.1 MBO With CliqueFlowmer

To test CliqueFlowmer's ability to conduct CMD through MBO, we use the following protocol. We sample N existing materials and encode them with the CliqueFlowmer encoder. Then, we optimize the materials' representations, using $T = 2000$ gradient steps (Equation (6)). The converged representations are then decoded with the CliqueFlowmer decoder, thus rendering N new materials (see Figure (3) for examples). Additionally, one can filter out the most promising candidates prior to their ground-truth evaluation. Namely, once optimization converges, one can predict the target property with the prediction head, $f_\theta(\mathbf{z})$, and select top-$k\%$ solutions with the best values. The attractiveness of this approach stems from the computational savings it offers—having run the cheap optimization stage in the latent space, one can reject the majority of suboptimal latents before passing the most promising ones to the expensive denoising and relaxation stages (Appendix I discusses the wall-clock time complexity of our method). We refer to this approach *CliqueFlowmer-Top* and set $k = 10$ in our experiments.

Metric	CrystalFormer	DiffCSP	DiffCSP++	MatterGen	**CliqueFlowmer**	**-Top**
E_{form} (↓)	0.71	0.59	0.65	0.60	-0.81	**-0.99**
Stable (↑)	14.1	19.2	**19.8**	18.5	14.5	13.6
S.U.N. (↑)	12.8	**18.6**	18.5	17.6	14.4	13.4
E_{form} / S.U.N. (↓)	1.06	1.02	1.10	0.98	-0.65	**-1.06**
Band Gap (↓)	0.52	0.63	0.48	0.57	**0.03**	0.07
Stable (↑)	14.1	19.2	19.8	18.5	61.3	**69.4**
S.U.N. (↑)	12.8	18.6	18.5	17.6	61.3	**69.4**
Band Gap / S.U.N. (↓)	0.37	0.55	0.23	0.40	**0.02**	0.05

Table 1: Target property values (Formation Energy and Band Gap), stability, and S.U.N. rate (percentage) across generative model baselines and MBO with our model. Best results in each row are in **bold**; second-best are underlined. **CliqueFlowmer** and CliqueFlowmer-**Top** reduce formation energy from the initial sample average of 0.46 to -0.81 and -0.99, respectively. The materials also achieve competitive stability and S.U.N. rates. Furthermore, among discovered S.U.N. materials, they achieve even lower property values (Eform / S.U.N) than the baselines. CliqueFlowmer and CliqueFlowmer-Top also reduce the band gap from the sample average of 0.57 to 0.03 and 0.07, respectively, while achieving superior stability and S.U.N. rates and property values among S.U.N. materials (Band Gap / S.U.N.). Thus, our models solve the optimization problem in Equation (1) while attaining high stability, novelty, and uniqueness of proposed materials. More metrics in Appendix G.

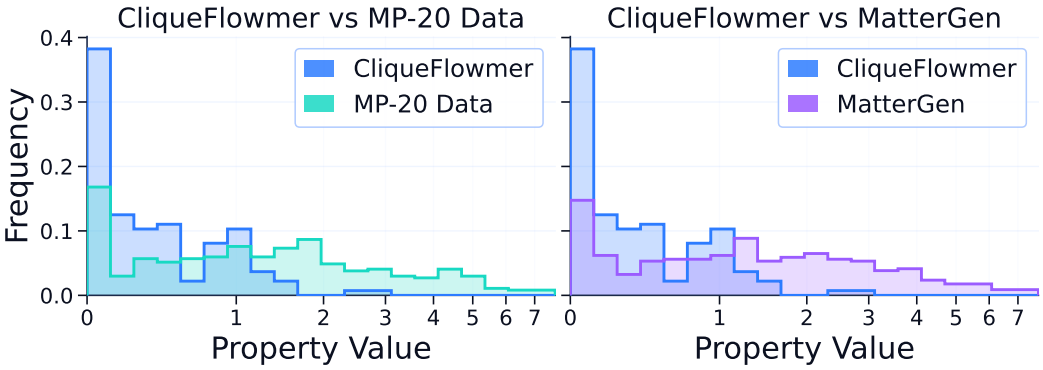

Figure 4: The distribution of the property value (band gap) among discovered materials. We compare CliqueFlowmer (blue) to materials from MP-20 dataset (green, *left*) and to those generated by MatterGen (purple, *right*). For all evaluations, we remove materials with $\Delta_{\text{band}} = 0$ (our model excels at discovering them without loss of S.U.N. metrics—see Table 1 for results and Appendix G) for better interpretability. We visualize the property in the log scale. Materials optimized by CliqueFlowmer have values accumulated near zero while others are more evenly spread out.

To test the success of this optimization procedure, we measure the target property value of the $N = 10^4$ original materials and the value of the newly-proposed ones. Additionally, to examine if our method produces both interesting and stable materials, we calculate the S.U.N. rate (stable, unique, novel) (Zeni et al., 2023) among the proposed solutions. Then, to study the optimization performance among the interesting materials, the target property is re-evaluated for examples that are classified as S.U.N. We compare our results to those of CrystalFormer (Taniai et al., 2024), DiffCSP (Jiao et al., 2023), DiffCSP++ (Jiao et al., 2024), and MatterGen (Zeni et al., 2023), whose generated structures we obtained from Kazeev et al. (2025). Due to computational limitations, we relax all the materials (including those from the baselines) approximately with M3GNet (Chen & Ong, 2022) and determine stability with energy above local hull[5]. To compensate for the bias induced by these approximations, we use the *strictly stable* criterion for stability (see Appendix A). Additionally, we provide modest evaluations with DFT in Appendix G.

Results in Table 1 and Figure (4) show that CliqueFlowmer drastically reduces the value of the target property (M3GNet formation energy & MEGNet band gap), significantly outperforming materials generated by the baselines. In the formation energy task, this quality is further amplified by CliqueFlowmer-Top, which reduces the objective value even further. We suspect that, in the band gap task, we do not observe this effect because the band gap is lower-bounded by zero, and

[5]As a result, our Stable and S.U.N. rates overestimate the true numbers but they do so for all methods.

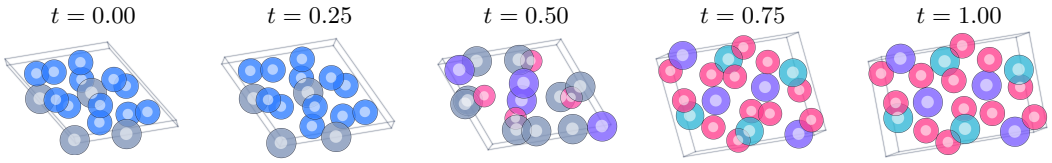

(a) As_3Rh (b) As_3Rh (c) $In_4Rh_9S_4$ (d) $MgInBr_3$ (e) $MgInBr_3$

Figure 5: **Latent interpolation between two materials.** We linearly interpolate $z^{(t)} = (1-t)z^{(0)} + tz^{(1)}$ between As_3Rh and $MgInBr_3$ and decode each $z^{(t)}$. The unit cells evolve smoothly in the cell shape, atom positions, and atom count.

thus the ordering of the top materials in the latent space may be driven by approximation errors. Furthermore, while the purpose of CliqueFlowmer is property optimization, the structures proposed by the model outperform the baselines in terms of the S.U.N. rate in the band gap optimization task. This may be surprising given that it is formation energy that is more tightly related to stability. However, it is known in materials science that simply minimizing the formation energy may lead to low-energy regions of the materials space with many competing phases, resulting in fewer stable materials (Riebesell et al., 2025). Furthermore, in both tasks, the S.U.N. materials from our method outperformed those from the baselines, in terms of the target property, regardless of the S.U.N. rate. Ultimately, the strong optimization performance (overall and /S.U.N) and high S.U.N. rates exceeded our expectations. We attribute this result to our careful construction of our domain-specific auto-encoder and conservative latent-space optimization (see Appendix F & J for more information).

4.2 Optimization Algorithm

As described in Section 3.5, having trained CliqueFlowmer, we discover new materials by solving the optimization problem from Equation (5). In this paper, we utilized the back-propagation-free ES algorithm (Salimans et al., 2017). This section provides an empirical justification of this counterintuitive choice. We compare the performance of the gradient derived by back-propagation (BP) to ES by optimizing $N = 100$ structures, in CliqueFlowmer's latent space, for $T = 1000$ steps. In our experiments, both gradients were applied by Adam optimization algorithm (Kingma, 2014), as well as by its decoupled weight decay variant (Loshchilov et al., 2017, BP+W, ES+W). Figure (6) shows that, instead of decreasing the minimized property, BP and BP+W have drastically increased it. Meanwhile, ES has successfully progressed towards the property minimization, and ES+W has done that most effectively. Thus, our main experiments use ES+W. For more information consult Appendix F.

4.3 Material Representations

The architecture of our model learns reparameterizations $\mathbf{z}$ of materials M that are meant to navigate the transdimensional space of materials smoothly. To demonstrate their ability to do so, we linearly interpolate two materials, $\mathsf{M}^{(0)}$ (As3Rh) and $\mathsf{M}^{(1)}$ (MgInBr3), by linearly mixing their representations $\mathbf{z}^{(0)}$ and $\mathbf{z}^{(1)}$,

$$\mathbf{z}^{(t)} = (1-t) \cdot \mathbf{z}^{(0)} + t \cdot \mathbf{z}^{(1)}.$$

We then decode the mixed representations and visualize the induced structures in Figure (5). We use Pymatgen's 2D plots for better clarity (Ong et al., 2013). The resulting materials gradually evolve from As3Rh into MgInBr3 by altering their composition, unit cell shape, and atom positions, supporting the claim that the latent space smoothly navigates the materials space. Such a result justifies an ablation verifying if one can obtain well-performing (in terms of $f(\mathsf{M})$) materials by "mixing" existing structures.

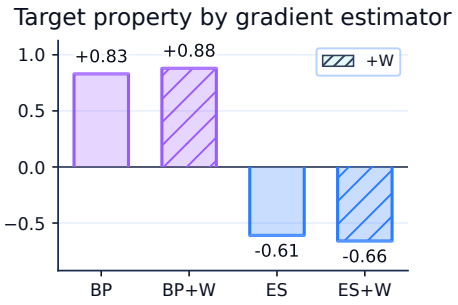

Figure 6: Comparison of gradient estimators—back-propagation (BP) vs. evolution strategies (ES), and weight decay. We plot the average change of the target property due to optimization, over 100 materials. Each algorithm performed 1000 steps, which was sufficient to reject back-propagation as divergent.

To quantify how promising that is, we sample $N_{\text{pair}} = 10$ pairs of existing materials and conduct an 8-step linear interpolation, at the same time evaluating $f(\mathsf{M})$ of the decoded, mixed structures. The results in Figure (7) show that the target property, unfortunately, tends to be higher along the interpolation trajectory. In particular, it reaches its apex in the middle of interpolation. Nevertheless, the failure of this naïve approach strengthens the motivation for more sophisticated tools, like MBO.

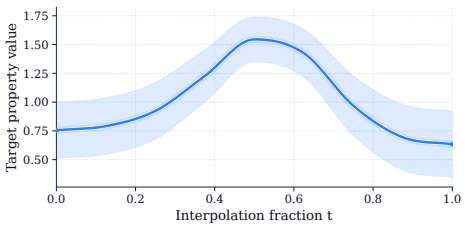

Figure 7: Average $f(\mathsf{M})$ (we used formation energy) with standard error of the mean (SEM) over the course of linear interpolation. The curve was smoothed out with the Gaussian kernel. The value tends to be higher along the interpolation trajectory.

Since the latent space of CliqueFlowmer was trained to follow a clique decomposition, we study how individual pieces of this structure impact the represented materials. Thus, we investigate how changes in individual cliques affect the observed material by interpolating a single clique between two examples, while keeping the rest of the representation fixed at one of the interpolated examples. That is, we fix two latent vectors, $\mathbf{z}^{(0)}$ and $\mathbf{z}^{(1)}$, and change only the coordinates of $\mathbf{z}^{(0)}$ that correspond to the cth clique,

$$\mathbf{Z}_c^{(t)} = (1-t) \cdot \mathbf{Z}_c^{(0)} + t \cdot \mathbf{Z}_c^{(1)}.$$

We visualize this analysis, for materials As3Rh and MgInBr3, and cliques 1 and 6 (out of 8), in Figure (8). The results reveal that these two cliques affect the material structure differently. In particular, alternating clique 1 (top row) does not affect the material decomposition much—on the other hand, it "lifts" two side Rhodium (Rh) atoms away from the bottom Rh atom. On the contrary, interpolating clique 6 (bottom row) does not simply modify the positions of the four Rh atoms, but it does eventually substitute them and Arsenic (As) atoms for Vanadium (V) atoms. This investigation supports a hypothesis that the learned cliques represent different properties of the materials' structure. Formalizing this relationship is not, however, the focus of this paper, so we leave it to future work.

5 Related Works

The cost and duration of computational materials discovery (CMD) has motivated research in automated methods (Jain et al., 2013). Recently, thanks to advancements in generative models, deep learning-based techniques of direct discovery through generation have become popular. Notably, Crystal Diffusion VAE (Xie et al., 2021, CDVAE) leverages diffusion models (Ho et al., 2020) to harness sampling of material representations learned by a variational auto-encoder (Kingma & Welling, 2013) which, unlike ours, are not equipped with a decomposable structure and transformer backbones. Similarly, FlowMM (Miller et al., 2024) utilizes flow-matching (Lipman et al., 2022) models to directly generate new materials. While that work's main focus is mathematically sound generative modeling on appropriate manifolds that materials are embedded in, we use flows as decoders of materials optimized in a latent space. Additionally, both of these models utilize the expensive equivariant graph neural networks based on spherical harmonics which, unlike efficient transformers, do not fit into the computational budget of many researchers (Li et al., 2025). Further, CrystalFormer (Taniai et al., 2024) generates materials auto-regressively, atom by atom. We generate atom species autoregressively in our model, but the geometry is generated with flow models. Most importantly, in our MBO model, these components are not the core generators, but they are just decoders of latent representations of optimized materials. MatterGen (Zeni et al., 2023), similarly to CDVAE, generates materials with diffusion models, and enables doing so conditioned on target properties. CliqueFlowmer, instead, directly optimizes the property value. Similarly to us, All-atom Diffusion Transformers (Joshi et al., 2025, ADiT) combine transformers and latent variables. In their architecture, however, the dimensionality of the latent variables depends on the atom count of the input material. This, in addition to not offering compression abilities, prevents employing MBO in the transdimensional materials space. Meanwhile, while completely dispensing with graph neural networks and spherical harmonics, CliqueFlowmer compresses materials into continuous, fixed-dimensional latent vectors which enables gradient-based search of the materials space.

There is a growing line of work in molecule discovery with diffusion models where the samplers are steered towards a target property-based Boltzmann distribution (Li et al.; Uehara et al., 2024; Tan et al., 2025; Liu et al., 2025). While these methods enable tilting the distribution of the target

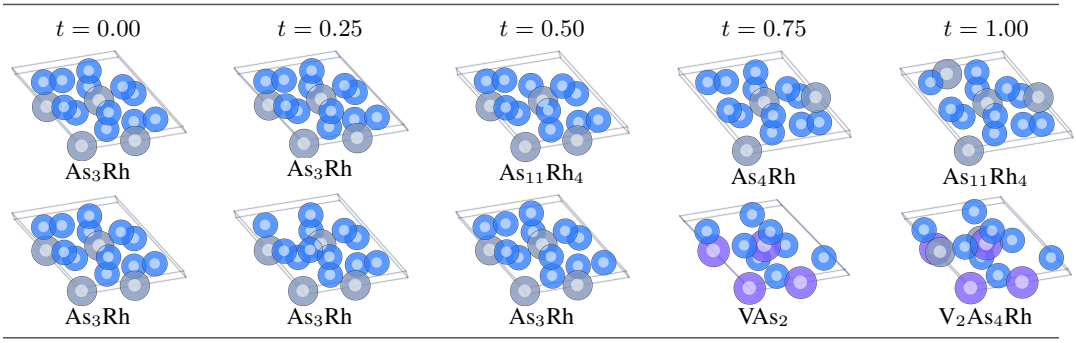

Figure 8: **Latent interpolation of cliques** between As_3Rh and $MgInBr_3$—2D visualization of primitive cells. *Top:* The studied clique does not significantly affect composition or the unit cell shape, but it does affect atom position and atom count slightly. In particular, it affects positions of two of the four Rh atoms that, eventually, from the bottom of the cell move to its top. *Bottom:* The clique does not alter the material geometry much, but it does significantly affect its composition by injecting Vanadium (V) atoms.

property to the desired side, we propose a method to directly optimize it in the space of chemical materials. Notably, MBO methods, such as MINs (Kumar & Levine, 2020), COMs (Trabucco et al., 2021), or MatchOpt (Hoang et al., 2025), aim at directly optimizing target property values. Among such methods, Cliqueformer (Kuba et al., 2024)—having introduced clique-based MBO into transformers—is most similar to our work. However, neither Cliqueformer nor prior MBO methods that introduce sophisticated algorithmic advancements are compatible with computational materials discovery (CMD) due to their simplistic neural network architectures suitable only for MBO benchmarks. Our work transcends these limitations by building a domain-specific model and learning algorithm that enables direct property optimization in CMD.

6 Conclusion

In this work, we proposed addressing the problem of computational materials discovery (CMD) with the tools from offline model-based optimization (MBO). We introduced CliqueFlowmer—a model that represents materials as continuous vectors and optimizes them with clique-based MBO. Our experimental results with CMD apparatus, such as MP-20 data and target property oracles, show that CliqueFlowmer enables efficient optimization of materials offline. The major limitation of our work is the impact of optimized properties—while the most easily measurable with oracles, they are not of the greatest interest of industrial labs that design materials for specialized applications. Together with increased access to oracles of more properties, we expect CliqueFlowmer to solve more impactful problems. Another limitation is the accuracy of our evaluation. For example, some works estimate properties of generated materials with software conducting (high-cost) density functional theory calculations which are known to be very accurate. Meanwhile we employed machine learning-based oracles in the majority of our evaluations. These can induce errors, as confirmed by our limited DFT checks. Overall, the most strongly validated conclusion of our study is that CliqueFlowmer is highly effective at offline property optimization; by contrast, absolute stability-based metrics such as S.U.N. are more sensitive to the surrogate-oracle stack and should be interpreted with greater caution. Lastly, we hope that this work will inspire the CMD community to add MBO to its toolkit.

Acknowledgements

Kuba Grudzien's research is supported by a grant from NSF AI4OPT AI Institute for Advances in Optimization (Award 2112533). Pieter Abbeel holds concurrent appointments as a Professor at UC Berkeley and as an Amazon Scholar. This paper describes work performed at UC Berkeley and is not associated with Amazon.

References

Achiam, J., Adler, S., Agarwal, S., Ahmad, L., Akkaya, I., Aleman, F. L., Almeida, D., Altenschmidt, J., Altman, S., Anadkat, S., et al. Gpt-4 technical report. *arXiv preprint arXiv:2303.08774*, 2023.

Chen, C. and Ong, S. P. A universal graph deep learning interatomic potential for the periodic table. *Nature Computational Science*, 2(11):718–728, 2022.

Chen, C., Ye, W., Zuo, Y., Zheng, C., and Ong, S. P. Graph networks as a universal machine learning framework for molecules and crystals. *Chemistry of Materials*, 31(9):3564–3572, 2019.

Chen, C.-T. and Gu, G. X. Generative deep neural networks for inverse materials design using backpropagation and active learning. *Advanced Science*, 7(5):1902607, 2020.

Esser, P., Kulal, S., Blattmann, A., Entezari, R., Müller, J., Saini, H., Levi, Y., Lorenz, D., Sauer, A., Boesel, F., et al. Scaling rectified flow transformers for high-resolution image synthesis. In *Forty-first international conference on machine learning*, 2024.

Freese, T., Elzinga, N., Heinemann, M., Lerch, M. M., and Feringa, B. L. The relevance of sustainable laboratory practices. *Rsc Sustainability*, 2(5):1300–1336, 2024.

Frohner, N., Gmys, J., Melab, N., Raidl, G., and Talbi, E.-G. Parallel beam search for combinatorial optimization. In *Workshop Proceedings of the 51st International Conference on Parallel Processing*, pp. 1–8, 2022.

Fu, J., Kumar, A., Nachum, O., Tucker, G., and Levine, S. D4rl: Datasets for deep data-driven reinforcement learning. *arXiv preprint arXiv:2004.07219*, 2020.

Glasserman, P. *Monte Carlo methods in financial engineering*, volume 53. Springer, 2004.

Gokcekuyu, Y., Ekinci, F., Guzel, M. S., Acici, K., Aydin, S., and Asuroglu, T. Artificial intelligence in biomaterials: a comprehensive review. *Applied Sciences*, 14(15):6590, 2024.

Grudzien, K., Uehara, M., Levine, S., and Abbeel, P. Functional graphical models: Structure enables offline data-driven optimization. In *International Conference on Artificial Intelligence and Statistics*, pp. 2449–2457. PMLR, 2024.

Han, N. and Su, B.-L. Ai-driven material discovery for energy, catalysis and sustainability. *National Science Review*, 12(5):nwaf110, 2025.

Havens, A., Miller, B. K., Yan, B., Domingo-Enrich, C., Sriram, A., Wood, B., Levine, D., Hu, B., Amos, B., Karrer, B., et al. Adjoint sampling: Highly scalable diffusion samplers via adjoint matching. *arXiv preprint arXiv:2504.11713*, 2025.

Hendrycks, D. and Gimpel, K. Gaussian error linear units (gelus). *arXiv preprint arXiv:1606.08415*, 2016.

Heyd, J., Scuseria, G. E., and Ernzerhof, M. Hybrid functionals based on a screened coulomb potential. *The Journal of Chemical Physics*, 118(18):8207–8215, 2003. doi: 10.1063/1.1564060.

Ho, J. and Salimans, T. Classifier-free diffusion guidance. *arXiv preprint arXiv:2207.12598*, 2022.

Ho, J., Jain, A., and Abbeel, P. Denoising diffusion probabilistic models. *Advances in Neural Information Processing Systems*, 33:6840–6851, 2020.

Hoang, M., Fadhel, A., Deshwal, A., Doppa, J. R., and Hoang, T. N. Learning surrogates for offline black-box optimization via gradient matching. *arXiv preprint arXiv:2503.01883*, 2025.

Hoare, C. A. R. Quicksort. *The Computer Journal*, 5(1):10–16, 1961.

Inizan, T. J., Kaplan, A., Yang, S., Lin, Y.-h., Abdelgaid, M., Yin, J., Zheng, Z., Mirzaei, S., Alawadhi, A. H., Cubuk, E. D., et al. Generative model for enhancing reticular material discovery. 2025. URL https://openreview.net/pdf?id=m8pGrT9WDa.

Jain, A., Ong, S. P., Hautier, G., Chen, W., Richards, W. D., Dacek, S., Cholia, S., Gunter, D., Skinner, D., Ceder, G., et al. Commentary: The materials project: A materials genome approach to accelerating materials innovation. *APL materials*, 1(1), 2013.

Jiao, R., Huang, W., Lin, P., Han, J., Chen, P., Lu, Y., and Liu, Y. Crystal structure prediction by joint equivariant diffusion. *Advances in Neural Information Processing Systems*, 36:17464–17497, 2023.

Jiao, R., Huang, W., Liu, Y., Zhao, D., and Liu, Y. Space group constrained crystal generation. *arXiv preprint arXiv:2402.03992*, 2024.

Joshi, C. K., Fu, X., Liao, Y.-L., Gharakhanyan, V., Miller, B. K., Sriram, A., and Ulissi, Z. W. All-atom diffusion transformers: Unified generative modelling of molecules and materials. *arXiv preprint arXiv:2503.03965*, 2025.

Kazeev, N., Levy, D., Jiao, R., Okhotin, A., Zhu, R., Nong, W., et al. Generated crystals for wyformer, diffcsp, diffcsp++, wycryst, symmcd, crystalformer, miad & mattergen. figshare Dataset, 2025. URL https://doi.org/10.6084/m9.figshare.29145101.v4.

Kingma, D. P. Adam: A method for stochastic optimization. *arXiv preprint arXiv:1412.6980*, 2014.

Kingma, D. P. and Welling, M. Auto-encoding variational bayes. *arXiv preprint arXiv:1312.6114*, 2013.

Kirklin, S., Saal, J. E., Meredig, B., Thompson, A., Doak, J. W., Aykol, M., Rühl, S., and Wolverton, C. The open quantum materials database (oqmd): assessing the accuracy of dft formation energies. *npj Computational Materials*, 1(1):1–15, 2015.

Kohn, W. and Sham, L. J. Self-consistent equations including exchange and correlation effects. *Physical review*, 140(4A):A1133, 1965.

Kuba, J. G., Abbeel, P., and Levine, S. Cliqueformer: Model-based optimization with structured transformers. *arXiv preprint arXiv:2410.13106*, 2024.

Kumar, A. and Levine, S. Model inversion networks for model-based optimization. *Advances in Neural Information Processing Systems*, 33:5126–5137, 2020.

Kumar, A., Zhou, A., Tucker, G., and Levine, S. Conservative q-learning for offline reinforcement learning. *Advances in Neural Information Processing Systems*, 33:1179–1191, 2020.

Kumar, A., Yazdanbakhsh, A., Hashemi, M., Swersky, K., and Levine, S. Data-driven offline optimization for architecting hardware accelerators. *arXiv preprint arXiv:2110.11346*, 2021.

Lei Ba, J., Kiros, J. R., and Hinton, G. E. Layer normalization. *ArXiv e-prints*, pp. arXiv–1607, 2016.

Li, X., Zhao, Y., Wang, C., Scalia, G., Eraslan, G., Nair, S., Biancalani, T., Ji, S., Regev, A., Levine, S., et al. Derivative-free guidance in continuous and discrete diffusion models with soft value-based decoding, 2024. *URL https://arxiv. org/abs/2408.08252*.

Li, Y., Huang, L., Ding, Z., Wei, X., Wang, C., Yang, H., Wang, Z., Liu, C., Shi, Y., Jin, P., et al. E2former: An efficient and equivariant transformer with linear-scaling tensor products. In *The Thirty-ninth Annual Conference on Neural Information Processing Systems*, 2025.

Lin, D.-Z., Pan, K.-J., Li, Y., Musgrave III, C. B., Zhang, L., Jayarapu, K. N., Li, T., Tran, J. V., Goddard III, W. A., Luo, Z., et al. A high-throughput experimentation platform for data-driven discovery in electrochemistry. *Science Advances*, 11(14):eadu4391, 2025.

Lipman, Y., Chen, R. T., Ben-Hamu, H., Nickel, M., and Le, M. Flow matching for generative modeling. *arXiv preprint arXiv:2210.02747*, 2022.

Liu, G.-H., Choi, J., Chen, Y., Miller, B. K., and Chen, R. T. Adjoint schr\" odinger bridge sampler. *arXiv preprint arXiv:2506.22565*, 2025.

Loshchilov, I., Hutter, F., et al. Fixing weight decay regularization in adam. *arXiv preprint arXiv:1711.05101*, 5, 2017.

Miller, B. K., Chen, R. T., Sriram, A., and Wood, B. M. Flowmm: Generating materials with riemannian flow matching. *arXiv preprint arXiv:2406.04713*, 2024.

Ong, S. P., Richards, W. D., Jain, A., Hautier, G., Kocher, M., Cholia, S., Gunter, D., Chevrier, V. L., Persson, K. A., and Ceder, G. Python materials genomics (pymatgen): A robust, open-source python library for materials analysis. *Computational Materials Science*, 68:314–319, 2013.

Park, H., Li, Z., and Walsh, A. Has generative artificial intelligence solved inverse materials design? *Matter*, 7(7):2355–2367, 2024.

Peebles, W. and Xie, S. Scalable diffusion models with transformers. In *Proceedings of the IEEE/CVF international conference on computer vision*, pp. 4195–4205, 2023.

Riebesell, J., Goodall, R. E., Benner, P., Chiang, Y., Deng, B., Ceder, G., Asta, M., Lee, A. A., Jain, A., and Persson, K. A. A framework to evaluate machine learning crystal stability predictions. *nature machine intelligence*, 7(6):836–847, 2025.

Salimans, T., Ho, J., Chen, X., Sidor, S., and Sutskever, I. Evolution strategies as a scalable alternative to reinforcement learning. *arXiv preprint arXiv:1703.03864*, 2017.

Shahzad, K., Mardare, A. I., and Hassel, A. W. Accelerating materials discovery: combinatorial synthesis, high-throughput characterization, and computational advances. *Science and Technology of Advanced Materials: Methods*, 4(1):2292486, 2024.

Shin, D.-H., Lee, D.-J., Son, Y.-H., and Kam, T.-E. Treatment stitching with schr\" odinger bridge for enhancing offline reinforcement learning in adaptive treatment strategies. *arXiv preprint arXiv:2511.12075*, 2025.

Sun, W., Dacek, S. T., Ong, S. P., Hautier, G., Jain, A., Richards, W. D., Gamst, A. C., Persson, K. A., and Ceder, G. The thermodynamic scale of inorganic crystalline metastability. *Science advances*, 2(11):e1600225, 2016.

Tan, C. B., Bose, A. J., Lin, C., Klein, L., Bronstein, M. M., and Tong, A. Scalable equilibrium sampling with sequential boltzmann generators. *arXiv preprint arXiv:2502.18462*, 2025.

Taniai, T., Igarashi, R., Suzuki, Y., Chiba, N., Saito, K., Ushiku, Y., and Ono, K. Crystalformer: Infinitely connected attention for periodic structure encoding. *arXiv preprint arXiv:2403.11686*, 2024.

Team, G., Georgiev, P., Lei, V. I., Burnell, R., Bai, L., Gulati, A., Tanzer, G., Vincent, D., Pan, Z., Wang, S., et al. Gemini 1.5: Unlocking multimodal understanding across millions of tokens of context. *arXiv preprint arXiv:2403.05530*, 2024.

Thiel, P. Paypal co-founder peter thiel warns of tech stagnation: 'without ai, there's just nothing going on'. *Economic Times*, 2025. URL https://economictimes.indiatimes.com/magazines/panache/paypal-co-founder-peter-thiel-warns-of-tech-stagnation-without-ai-theres-just-nothing-going-o articleshow/122141331.cms.

Trabucco, B., Kumar, A., Geng, X., and Levine, S. Conservative objective models for effective offline model-based optimization. In *International Conference on Machine Learning*, pp. 10358–10368. PMLR, 2021.

Trabucco, B., Geng, X., Kumar, A., and Levine, S. Design-bench: Benchmarks for data-driven offline model-based optimization. In *International Conference on Machine Learning*, pp. 21658–21676. PMLR, 2022.

Uehara, M., Zhao, Y., Hajiramezanali, E., Scalia, G., Eraslan, G., Lal, A., Levine, S., and Biancalani, T. Bridging model-based optimization and generative modeling via conservative fine-tuning of diffusion models. *arXiv preprint arXiv:2405.19673*, 2024.

Vaswani, A., Shazeer, N., Parmar, N., Uszkoreit, J., Jones, L., Gomez, A. N., Kaiser, Ł., and Polosukhin, I. Attention is all you need. *Advances in neural information processing systems*, 30, 2017.

Wierstra, D., Schaul, T., Glasmachers, T., Sun, Y., Peters, J., and Schmidhuber, J. Natural evolution strategies. *The Journal of Machine Learning Research*, 15(1):949–980, 2014.

Wu, Y., Schuster, M., Chen, Z., Le, Q. V., Norouzi, M., Macherey, W., Krikun, M., Cao, Y., Gao, Q., Macherey, K., et al. Google's neural machine translation system: Bridging the gap between human and machine translation. In *Proceedings of the 2016 Conference on Empirical Methods in Natural Language Processing (EMNLP)*, 2016.

Xie, T., Fu, X., Ganea, O.-E., Barzilay, R., and Jaakkola, T. Crystal diffusion variational autoencoder for periodic material generation. *arXiv preprint arXiv:2110.06197*, 2021.

Yan, Y., Hu, F., Chen, J., Bhendawade, N., Ye, T., Gong, Y., Duan, N., Cui, D., Chi, B., and Zhang, R. Fastseq: Make sequence generation faster. In *Proceedings of the 59th Annual Meeting of the Association for Computational Linguistics and the 11th International Joint Conference on Natural Language Processing: System Demonstrations*, pp. 218–226, 2021.

Yang, S., Batzner, S., Gao, R., Aykol, M., Gaunt, A. L., McMorrow, B., Rezende, D. J., Schuurmans, D., Mordatch, I., and Cubuk, E. D. Generative hierarchical materials search. *arXiv preprint arXiv:2409.06762*, 2024.

Zeni, C., Pinsler, R., Zügner, D., Fowler, A., Horton, M., Fu, X., Shysheya, S., Crabbé, J., Sun, L., Smith, J., et al. Mattergen: a generative model for inorganic materials design. *arXiv preprint arXiv:2312.03687*, 2023.

Zeni, C., Pinsler, R., Zügner, D., Fowler, A., Horton, M., Fu, X., Wang, Z., Shysheya, A., Crabbé, J., Ueda, S., et al. A generative model for inorganic materials design. *Nature*, 639(8055):624–632, 2025.

Appendix

Contents

A Additional Background **17**

A.1 Computational Materials Discovery Practices 17

A.2 Next-Token Prediction with Transformers 17

A.3 Beam Search 17

A.4 Functional Graphical Models and Clique-Based Representations 18

B Evolution Strategies **18**

C Classifier-Free Guidance for Diffusion and Flow Models **19**

D Flow Conditioning Via Cross-Attention **20**

E Prior Distribution Of Lattice Lengths **21**

F Optimization Algorithm Tuning **21**

G More Experimental Details **24**

H Lifted Logit-Normal Distribution **26**

I Inference Time Analysis **26**

J Model and Optimization Hyperparameters **28**

A Additional Background

This section provides additional background that helps understand the contribution of our work.

A.1 Computational Materials Discovery Practices

Computational materials discovery (CMD) aims to identify materials M whose physical or chemical properties, often, optimize a desired objective $f(\mathsf{M})$, such as formation energy or electronic behavior. Simultaneously, the materials should be thermodynamically stable in order to be plausible to synthesize. Stability can be determined by calculating the structure's energy above hull E_{hull}, which can be done with density functional theory (Kohn & Sham, 1965, DFT) calculations and a reference set in form of a convex hull. A material is (strictly) *stable* if its energy above hull is non-positive $E_{\text{hull}}(\mathsf{M}) \leq 0$. Nevertheless, in practice, many materials with slightly positive $E_{\text{hull}} \in (0, 0.1]$eV/atom are synthesizable as well. To account for this phenomenon, a material is said to be *metastable* if its energy above hull is at most 0.1 eV/atom (Jain et al., 2013; Kirklin et al., 2015; Sun et al., 2016). The MP-20 dataset used in this work consists of metastable materials (Xie et al., 2021). Evaluating candidate materials using first-principles methods such as density DFT is accurate but computationally expensive, motivating the construction of large offline datasets such as the Materials Project (Jain et al., 2013).

Recent machine-learning approaches to CMD broadly fall into two categories. *Surrogate modeling* methods learn predictors of material properties and use them for screening or ranking candidates. *Generative modeling* methods—based on VAEs, diffusion models, or flows—learn to sample new materials resembling those in a reference dataset (Xie et al., 2021; Zeni et al., 2023; Taniai et al., 2024). While generative models can produce valid and diverse structures, their likelihood-based training objective concentrates probability mass near the empirical data distribution, limiting their ability to aggressively explore property-optimal regions.

Offline model-based optimization (MBO) offers an alternative paradigm by directly optimizing a learned surrogate objective using only offline data (Kumar et al., 2020; Trabucco et al., 2022). Applying MBO to CMD is challenging due to the hybrid discrete-continuous structure of materials and their transdimensionality. CliqueFlowmer addresses this challenge by learning a fixed-dimensional latent representation of materials that admits structured optimization and can be decoded back into valid crystal structures.

A.2 Next-Token Prediction with Transformers

Next-token prediction is a standard training paradigm for autoregressive sequence models, including transformers (Vaswani et al., 2017). Given a sequence of discrete tokens $(x_1, \ldots, x_T)$, a causal transformer models the factorized distribution

$$p(\mathrm{x}_1, \ldots, \mathrm{x}_T) = \prod_{t=1}^{T} p(\mathrm{x}_t \mid \mathrm{x}_{<t}),$$

and is trained by minimizing the negative log-likelihood of each token conditioned on its prefix.

In CliqueFlowmer, next-token prediction is used to model the sequence of atom types in a material. Each structure is represented as a variable-length sequence augmented with explicit ⟨Start⟩ and ⟨Stop⟩ tokens. The autoregressive transformer is conditioned on the latent representation via adaptive layer normalization (AdaLN) (Peebles & Xie, 2023), allowing global structural information to influence all token predictions. This approach provides a flexible mechanism for handling discrete, variable-length outputs while integrating naturally with transformer architectures and beam search at generation time.

A.3 Beam Search

Beam search Wu et al. (2016) is a heuristic decoding algorithm for approximately maximizing the joint probability of an output sequence under an autoregressive model. Given a conditional next-token distribution $p_\theta(\mathrm{x}_k \mid \mathbf{x}_{<k})$, beam search maintains a set (the *beam*) of the top-K partial hypotheses at

each step, scored by accumulated log-probability,

$$s(\mathbf{x}_{1:k}) \;=\; \sum_{i=1}^{k} \log p_\theta(\mathrm{x}_i \mid \mathbf{x}_{<i}).$$

At the index k, each hypothesis in the beam is expanded by all (or a pruned subset of) next-token candidates, producing a pool of new hypotheses; the top-N_{beam} by score are retained. Decoding terminates when all hypotheses have emitted the ⟨Stop⟩ token, or when a maximum length is reached, and the best completed sequence is returned.

In CliqueFlowmer, we apply beam search to decode the discrete atom-type sequence from the autoregressive transformer conditioned on the optimized latent representation, using beam width $N_{\text{beam}} = 10$. This decoding step is used after latent-space optimization to produce a high-likelihood composition consistent with the latent code, before sampling the continuous geometry with the flow-based decoder.

A.4 Functional Graphical Models and Clique-Based Representations

CliqueFlowmer builds on the framework of *functional graphical models* introduced by Grudzien et al. (2024). In this framework, the target function of interest is modeled as an additive decomposition over overlapping cliques of latent variables. Concretely, a latent vector $\mathbf{z} \in \mathbb{R}^{d_z}$ is reshaped into a chain of overlapping cliques

$$\mathbf{Z} = \texttt{chain}(\mathbf{z}, d_{\text{clique}}, d_{\text{knot}})$$

where each clique shares a subset of variables (knots) with its neighbors. The surrogate objective is then parameterized as

$$f_\theta(\mathbf{z}) = \sum_{c=1}^{N_{\text{cliques}}} f_\theta(\mathbf{Z}_c, c),$$

where each term depends only on a local clique.

This structured decomposition induces a functional graphical model in which each clique corresponds to a factor, enabling *compositional generalization*. In particular, clique-based models support *stitching*: optimal in-distribution configurations of individual cliques can be recombined to form globally competitive solutions (Fu et al., 2020; Kuba et al., 2024). This property has been shown to substantially improve the effectiveness of offline MBO in high-dimensional design spaces.

In CliqueFlowmer, this clique structure is imposed on the latent representation of materials, enabling gradient-based or derivative-free optimization directly in latent space while maintaining a strong inductive bias toward in-distribution solutions. The decoder then maps optimized latent variables back into discrete atom types and continuous geometries, allowing clique-based MBO to operate over the transdimensional space of materials.

B Evolution Strategies

Evolution Strategies (ES) are a class of black-box optimization methods that estimate gradients of an expected objective using random perturbations of the parameters rather than back-propagation through the objective itself. In the scalable formulation introduced by Salimans et al. (2017), ES optimizes parameters $\phi \in \mathbb{R}^d$ by minimizing the smoothed objective

$$F(\phi) = \mathbb{E}_{\epsilon\sim\mathcal{N}(0,I)}\big[f(\phi + \sigma\epsilon)\big], \tag{7}$$

where σ controls the perturbation scale. The gradient of $F(\phi)$ can be estimated via Monte Carlo sampling thanks to the following identity,

$$\nabla_\phi F(\phi) = \frac{1}{\sigma}\mathbb{E}_{\epsilon\sim\mathcal{N}(0,I)}\big[f(\phi + \sigma\epsilon)\epsilon\big]$$

and used in a standard stochastic gradient descent loop. In our work, we substitute a representation $\mathbf{z}$ of a material M into the place of ϕ, and we minimize the expected perturbed approximation $f_\theta(\mathbf{z})$ of the target property.

Rank-Based ES. A key practical component of modern ES is *rank-based fitness shaping*. Instead of using raw function values $f(\phi + \sigma\epsilon_i)$, ES replaces them with normalized ranks computed across the population of perturbations. For example, if the values of, say 3, perturbed parameters $(\phi + \sigma\epsilon_1, \phi + \sigma\epsilon_2, \phi + \sigma\epsilon_3)$ are $(10, -1, 5)$, then the values are turned into ranks $(3, 1, 2)$. Then, they are standardized to have mean zero and unit variance, ultimately taking on values $(-\sqrt{1.5}, 0, \sqrt{1.5})$. This transformation makes the update invariant to monotone rescalings of the objective, improves robustness to outliers and heavy-tailed noise, and stabilizes optimization when the scale of f varies over time (Salimans et al., 2017; Wierstra et al., 2014). As a result, ES behaves less like a noisy gradient estimator and more like a robust search-direction method.

Antithetic Sampling. To further reduce estimator variance, ES commonly employs *antithetic sampling*. For each sampled perturbation ϵ_i, its negation $-\epsilon_i$ is also evaluated, producing paired function values $f(\phi + \sigma\epsilon_i)$ and $f(\phi - \sigma\epsilon_i)$. The gradient estimate aggregates these symmetric evaluations. In the function value case, this causes odd-order noise terms to cancel in expectation and significantly reducing variance. When used with ranks, it verifies for each perturbation whether to go along or against the direction it points to.

For completeness, we write down the rank-based ES estimator with antithetic sampling for N_{pert} perturbations. First, note that each perturbation ϵ produces values $f(\phi + \sigma\epsilon)$ and $f(\phi - \sigma\epsilon)$, resulting in $2N_{\text{pert}}$ values from all perturbations. We rank all these values in the ascending order (the lowest value gets the lowest rank). Then, for clarity, we rank the perturbations ϵ based off the ranks of $f(\phi + \sigma\epsilon)$ (where the perturbation) was added, giving $\epsilon^1, \ldots, \epsilon^{N_{\text{pert}}}$. Let $r(i, +)$ and $r(i, -)$ be the ranks of $f(\phi + \sigma\epsilon^i)$ and $f(\phi - \sigma\epsilon^i)$ among all values. Then, let R^i_+ and R^i_- be their standardized versions. The final estimator takes form

$$\hat{\nabla}^{\text{ES}}(\phi) = \frac{1}{2\sigma \cdot N_{\text{pert}}} \sum_{i=1}^{N_{\text{pert}}} \left(R^i_+ - R^i_-\right)\epsilon^i. \tag{8}$$

Antithetic sampling effectively doubles sample efficiency and is especially beneficial in high-dimensional settings (Salimans et al., 2017; Glasserman, 2004).

Together, rank-based fitness shaping and antithetic sampling enable ES to scale to millions of parameters while remaining simple, highly parallelizable, and entirely gradient-free, making it a compelling alternative when back-propagation is unavailable, unreliable, or misleading (like in our case).

C Classifier-Free Guidance for Diffusion and Flow Models

Classifier-free guidance (CFG) is a technique originally introduced in the context of diffusion models to control the trade-off between sample quality and diversity without requiring an explicit classifier (Ho & Salimans, 2022). The key idea is to train a single conditional generative model that can operate both conditionally and unconditionally, and to combine the two modes at sampling time to bias generation toward the conditioning signal.

Formally, let $V_\theta(\mathbf{x}_t, t \mid c)$ denote a diffusion or flow model conditioned on some context c, and let $V_\theta(\mathbf{x}_t, t \mid \varnothing)$ denote the same model evaluated without conditioning. Classifier-free guidance constructs a guided vector field

$$V^\omega_\theta(\mathbf{x}_t, t \mid c) = (1 + \omega)\, V_\theta(\mathbf{x}_t, t \mid c) \;-\; \omega\, V_\theta(\mathbf{x}_t, t \mid \varnothing),$$

where $\omega \geq 0$ is the guidance strength. Increasing ω amplifies features correlated with the conditioning signal, at the cost of reduced diversity and potential distributional shift. Of course, $\omega = 0$ is equivalent to not using CFG—it corresponds to the vanilla Euler method.

While CFG was originally developed for diffusion models, the same principle applies directly to continuous normalizing flows and flow-matching models, where the learned vector field defines an ordinary differential equation (ODE) rather than a stochastic reverse process (Lipman et al., 2022). In this setting, guidance modifies the deterministic velocity field used during integration, biasing trajectories toward regions favored by the conditioning signal.

CFG in CliqueFlowmer. In CliqueFlowmer, classifier-free guidance is used during decoding of material geometry with the flow-matching model. The conditioning signal is the optimized latent

Table 2: Effect of classifier-free guidance strength on encode–decode consistency.

Guidance strength ω	Match ratio (%)
0	71
2	**80**
4	77

Table 3: Effect (match ratio in %) of cross-attention on encode–decode consistency.

Conditioning	$\omega = 0$	$\omega = 2$	$\omega = 4$
Flat	63	45	32
Cross-attention	71	**80**	77

representation $\mathbf{z}$, while the unconditional model is obtained by replacing $\mathbf{z}$ with Gaussian noise $\varepsilon_z \sim \mathcal{N}(0, I)$. During sampling, the guided vector field is integrated from $t = 0$ to $t = 1$ using an explicit ODE solver.

Reconstruction Experiment. To study the effect of guidance strength, we conducted an encode–decode consistency experiment. Given a material M, we encoded it into a latent representation $\mathbf{z}$ using the CliqueFlowmer encoder and then decoded it back into a material $\hat{\mathsf{M}}$ using the geometry flow with different guidance strengths $\omega \in \{0, 2, 4\}$. We then evaluated whether M and $\hat{\mathsf{M}}$ represent the same crystal structure using `StructureMatcher` from `pymatgen`, which accounts for lattice symmetries, atomic species, and fractional coordinates.

We report the *match ratio*, defined as the fraction of decoded structures that were deemed equivalent to their original inputs, over the sample of 100 structures. Results are shown in Table 2.

Discussion. Moderate classifier-free guidance ($\omega = 2$) substantially improves reconstruction fidelity compared to no guidance, indicating that conditioning on the latent representation is underutilized without explicit amplification. However, excessive guidance ($\omega = 4$) degrades performance, likely due to over-sharpening of the vector field and reduced robustness to modeling errors. This behavior mirrors observations in diffusion-based image and molecule generation, where intermediate guidance strengths often yield the best balance between faithfulness and stability (Ho & Salimans, 2022).

Based on these results, all main experiments in this work use a guidance strength of $\omega = 2$ during geometry decoding.

D Flow Conditioning Via Cross-Attention

The simplest way to condition the flow denoiser is, just as in the case of the atom-type decoder, via adaptive layer-norm that employs the flat representation $\mathbf{z} \in \mathbb{R}^{d_{\mathbf{z}}}$ (Peebles & Xie, 2023, AdaLN). Throughout the architecture's development, we tested our design choices with the reconstruction experiment from Appendix C. That is, by studying the rate at which we can encode a material M and decode it into $\hat{\mathsf{M}}$, so that the two match. In those experiments, the "flat" conditioning with AdaLN performed poorly. A breakthrough came from employing cross-attention as a form of conditioning (Vaswani et al., 2017). That is, we would use the clique form of the latent, $\mathbf{Z} \in \mathbb{R}^{N_{\text{clique}} \times d_{\text{clique}}}$, and treat it as if it was a sequence of hidden states. We would then insert a cross-attention layer between the actual flow transformer's hidden states and this "sequence" between the regular attention and feed-forward layers (Vaswani et al., 2017).

We examined both conditioning schemes in the reconstruction task with different CFG strengths and present the results in Table 3. The results indicate that cross-attention conditioning delivers superior reconstruction quality. Notably, the lowest match ratio recorded with cross-attention (71%) is higher than the highest match ratio of flat conditioning (63%). Furthermore, cross-attention conditioning displayed much lower volatility to CFG strength (the range of results being $80\% - 71\% = 9\%$) than flat conditioning ($63\% - 32\% = 31\%$). In our final experiments, we used a transformer flow denoiser with cross-attention.

E Prior Distribution Of Lattice Lengths

When we decode the geometry $\mathbf{G}$ of a material represented by $\mathbf{z}$ with composition $\mathbf{a}$, we initialize it with a sample from a prior distribution

$$p_0(\mathbf{G}|\mathbf{a}) = p_0^{\text{len}}(a, b, c|\mathbf{a}) \cdot p_0^{\text{ang}}(\alpha, \beta, \gamma|\mathbf{a}) \cdot p_0^{\text{pos}}(\mathbf{X}|\mathbf{a}). \tag{9}$$

Similarly to Miller et al. (2024), we chose to model $p_0^{\text{len}}(a, b, c|\mathbf{a}) = p_0^a(a|\mathbf{a}) \cdot p_0^b(b|\mathbf{a}) \cdot p_0^c(c|\mathbf{a})$ as an independent log-normal distribution. That is, for every $l \in \{a, b, c\}$, we consider it transformation of a variable l_{nor} via the logarithmic function,

$$l = \exp(l_{\text{nor}}) \quad \text{equiv.} \quad l_{\text{nor}} = \log(l) \tag{10}$$

and we model l_{nor} as normally distributed, $l_{\text{nor}} \sim \mathcal{N}(\mu_1, \sigma_l^2)$.

That said, we introduce a small modification that accounts for the physical meaning of this distribution. First, we recall that the volume of material M's unit cell is

$$\text{Vol}(\mathsf{M}) = abc \cdot \sqrt{1 - \cos^2\alpha - \cos^2\beta - \cos^2\gamma + 2\cos\alpha\cos\beta\cos\gamma} \;\propto\; abc. \tag{11}$$

The distribution we described in Equations (9) & (10) does not account for the number of atoms that the initialized unit cell is meant to fit. Meanwhile, materials with more atoms clearly need larger, in terms of volume, cells. To impose it, we introduce a simple change—we modify our prior distribution so that the average atom density,

$$\text{Den}(\mathsf{M}) = \frac{N_{\text{atom}}}{\text{Vol}(\mathsf{M})} \propto \frac{N_{\text{atom}}}{abc}. \tag{12}$$

is invariant to the atom count. We accomplish that by constructing *canonical* lattice lengths, $(\underline{a}, \underline{b}, \underline{c})$, such that $\text{Vol}(\mathsf{M}) \propto N_{\text{atom}}\underline{abc}$, and thus

$$\text{Den}(\mathsf{M}) = \frac{N_{\text{atom}}}{\text{Vol}(\mathsf{M})} \propto \frac{N_{\text{atom}}}{N_{\text{atom}}\underline{abc}} = \frac{1}{\underline{abc}}. \tag{13}$$

To construct them, simply, for each variable $l \in \{a, b, c\}$, we define

$$\underline{l} = \frac{1}{\sqrt[3]{N_{\text{atom}}}} \cdot l \quad \text{equiv.} \quad l = \sqrt[3]{N_{\text{atom}}} \cdot \underline{l},$$

which immediately gives us Equation (13). From then on, we model the canonical lengths as log-normal and estimate their distribution parameters (normal mean and standard deviation from data).

We investigated if this prior fits the data better. Namely, we estimated the distribution of the lattice lengths in two ways—*(1)* without the canonical (atom count-aware) transformation, and *(2)* with the canonical transformation. In (1), the lengths were modeled as log-normal, and in (2), they were modeled as atom count-scaled log-normal variables. We demonstrate the improved quality of method (2) in Figure (9).

F Optimization Algorithm Tuning

We verified, in Section 4.2 (Figure (6), that latent-space optimization of materials with backpropagation-based (BP) gradients diverges and gradients based on rank-based evolution strategies (Salimans et al., 2017, ES) are effective. In this section, we investigate this phenomenon deeper and ablate the weight decay strength of Adam optimization that we use (Kingma, 2014; Loshchilov et al., 2017). First, we discuss the failure of back-propagation (BP) from Section 4.2. It is known that MBO algorithms are sensitive to distribution shift, wherein optimized designs $\mathbf{x}$ become inputs to a predictive model $f_\theta(\mathbf{x})$ that makes erroneous predictions about them (Kumar & Levine, 2020; Kumar et al., 2020; Trabucco et al., 2021). Meanwhile, back-propagation is the most exact way of calculating the steepest direction of change with respect to such an imprecise function approximator. As a result, a gradient-based algorithm that fully "trusts" this estimator, commits to the artifacts of its errors, leading to poor designs (see Figure (10) for intuition).

To choose the final value of weight decay λ, we tested the value of the target property and the stability rate of materials (fraction of materials below the convex hull) it delivers. We evaluated weight

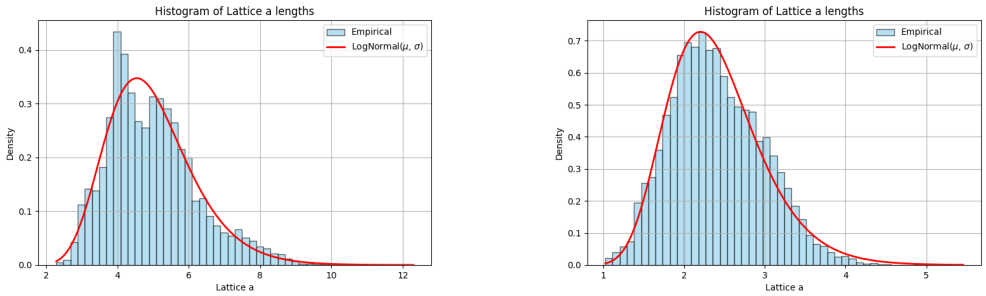

Figure 9: Two ways to model the distribution of lattice lengths, demonstrated on variable a. In the first scheme (left), the length is naively modeled as log-normally distributed. In the second, final scheme (right), the length is scaled down by the cubic root of the atom count, and the canonical length is modeled as a logit-normal variable. The log-normal density (red) fits the histogram (blue) better in the canonical case (right).

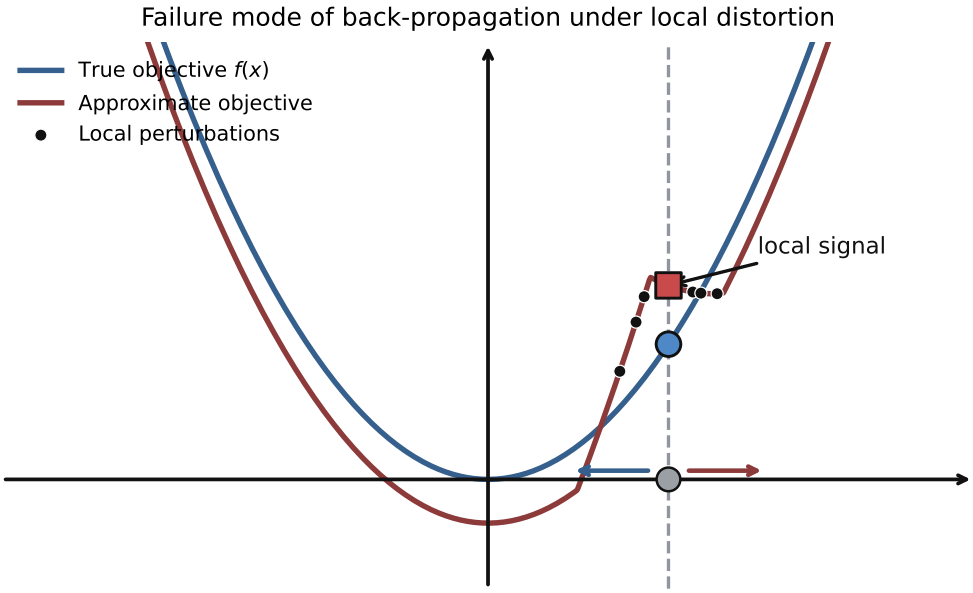

Figure 10: Intuition behind performance discrepancy between BP and ES. The function approximator (red) of the ground truth function (blue) has an artifact that is inconsistent with the ground truth. Near that artifact's location (gray), the derivative of the approximator (taken with respect to the red square) points updating to the right. Meanwhile, exploring the region with ES allows to identify the correct (left) update direction. The predicted values of the perturbed points are, from left to right: 0.99, 1.44, 1.67, 1.71, 1.70, and 1.70

decay values $\lambda \in \{0, 0.1, 0.2, 0.3, 0.4, 0.5\}$ by applying them to ES and AdamW in a process of optimization of $N = 100$ random materials (with M3GNet relaxation). We note that we could use more materials to get more accurate estimates, but that would be computationally costly and thus, potentially, not scalable. This time, we stress-tested the algorithms and ran $T = 2000$ optimization steps (twice as many as in Section 4.2). As a result, we found higher values of λ more effective at optimizing the target property and material stability. Ultimately, we found $\lambda = 0.4$ to offer the most promising compromise between the target property and stability and thus use it in our experiments.

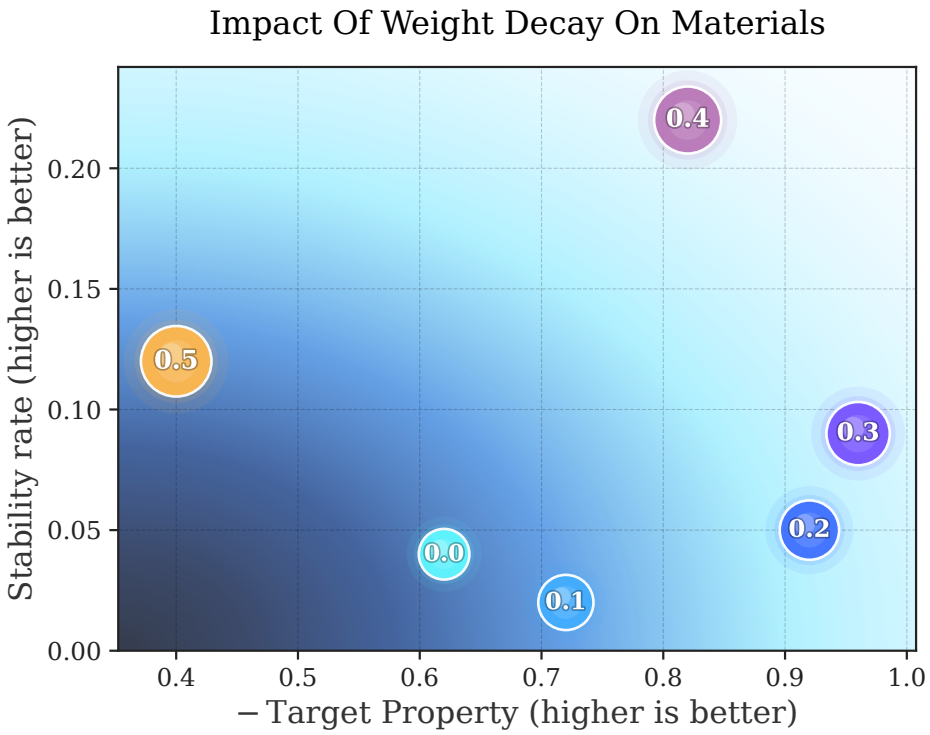

Figure 11: Ablation of the weight decay strength λ in the latent-space optimization algorithm. Weight decay $\lambda = 0.4$ delivers the strongest compromise between target property values and stability.

Metric	CrystalFormer	DiffCSP	DiffCSP++	MatterGen	**CliqueFlowmer**	**-Top**
E_{form} (↓)	0.71	0.59	0.65	0.60	-0.81	**-0.99**
Metastable (↑)	47.1	55.5	50.2	**57.0**	26.0	24.1
Stable (↑)	14.1	19.2	**19.8**	18.5	14.5	13.6
Unique (↑)	99.6	99.8	99.8	**100**	99.5	99.6
Novel (↑)	70.7	96.9	83.8	86.0	99.5	**99.6**
S.U.N. (↑)	12.8	**18.6**	18.5	17.6	14.4	13.4
E_{form} / S.U.N. (↓)	1.06	1.02	1.10	0.98	-0.65	**-1.06**
Band Gap (↓)	0.52	0.63	0.48	0.57	**0.03**	0.07
Metastable (↑)	47.1	55.5	50.2	57.0	**99.9**	99.7
Stable (↑)	14.1	19.2	19.8	18.5	61.3	**69.4**
Unique (↑)	99.6	99.8	99.8	**100**	**100**	**100**
Novel (↑)	70.7	96.9	83.8	86.0	**100**	**100**
S.U.N. (↑)	12.8	18.6	18.5	17.6	61.3	**69.4**
Band Gap / S.U.N. (↓)	0.37	0.55	0.23	0.40	**0.02**	0.05

Table 4: Target property values (Formation Energy and Band Gap), metastability, stability, uniqueness, novelty, and S.U.N. rate (percentage) across generative model baselines and MBO with our model. Best results in each row are in **bold**; second-best are underlined. We observe that, apart from superior property values, in each task, **CliqueFlowmer** and CliqueFlowmer**-Top** attain a very high (near or equal to 100%) novelty rate. This result satisfies our motivation for development of CMD methods that incorporate MBO and explore the materials space more aggressively than generative baselines.

Metric	CrystalFormer	DiffCSP	DiffCSP++	MatterGen	**CliqueFlowmer**	**-Top**
Eform (↓)	-0.59	-0.56	-0.47	-0.68	-2.43	**-2.87**
S.U.N.* (↑)	**56.63**	35.53	37.50	47.50	12.24	4.00
S.U.N. (↑)	**18.07**	2.63	7.95	7.50	2.04	0.00
Eform / S.U.N.* (↓)	-0.62	-0.64	-0.76	-0.84	-0.99	**-2.79**
Band Gap (↓)	0.81	0.86	0.77	1.00	0.20	**0.17**
S.U.N.* (↑)	**56.63**	35.53	37.50	47.50	2.04	3.09
S.U.N. (↑)	**18.07**	2.63	7.95	7.50	0.00	0.00
Band Gap / S.U.N.* (↓)	0.81	0.78	1.01	1.37	**0.11**	0.28

Table 5: Target property values (formation energy and band gap) and the S.U.N. rate, computed with DFT, for 100 structures with the lowest energy above hull according to M3GNet. We write S.U.N.* when we counted metastable materials as stable, and S.U.N. when we only used strictly stable materials.

G More Experimental Details

Additional metrics. In addition to the metrics provided in Table 1, we report the metastable rate, uniqueness rate, and novelty rate, of materials provided by the studied models, in Table 4. Materials that satisfy these three properties (stability, uniqueness, and novelty), are counted in while computing the S.U.N. rate that we report in Section 4.

DFT evaluations. Due to resource constraints, our full-scale evaluations in Tables 1 & 4 were done with machine learning oracles, such as M3GNet and MEGNet. To ground these results in rigorous physics, however, we have also conducted density functional theory (Kohn & Sham, 1965, DFT) evaluations of proposed materials. Namely, for each method evaluated in Section 4, we selected the 100 most stable structures (100 structures with the lowest E_{hull} values), as predicted by M3GNet. Then, we relaxed them with DFT and computed the target property values (formation energy and band gap). For band gap calculations, we used the approximate HSE (Heyd et al., 2003). The results in Table 5 show that CliqueFlowmer retains a strong advantage on the optimized property under DFT evaluation, confirming the central optimization result of the paper. At the same time, the DFT reevaluation reveals that stability-based metrics such as S.U.N. are substantially more sensitive to bias in the machine-learning oracle pipeline used for development and candidate selection. As a result, the S.U.N. (and S.U.N.*) rates of materials proposed by our method are much lower than we previously estimated. Nevertheless, among S.U.N.* materials, CliqueFlowmer delivers the most optimal structures. With enhanced DFT infrastructure for development and higher-quality data, we expect CliqueFlowmer to improve its ability to deliver optimized and stable materials.

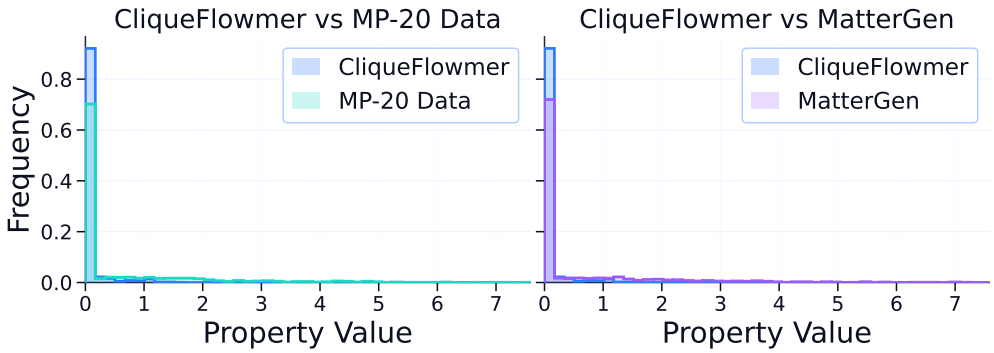

Figure 12: Full version of Figure (4). Our method puts significant weight on $\Delta_{\text{band}} = 0$ materials.

Histogram of unprocessed band gaps. Figure 12 presents the unfiltered histogram of band gap values in the band gap optimization task. Both CliqueFlowmer and the reference materials put a substantial probability mass on near-zero band gap materials, obstructing interpretation of the histograms. Hence, Figure 4 in Section 4 filtered out materials with $\Delta_{\text{band}} = 0$.

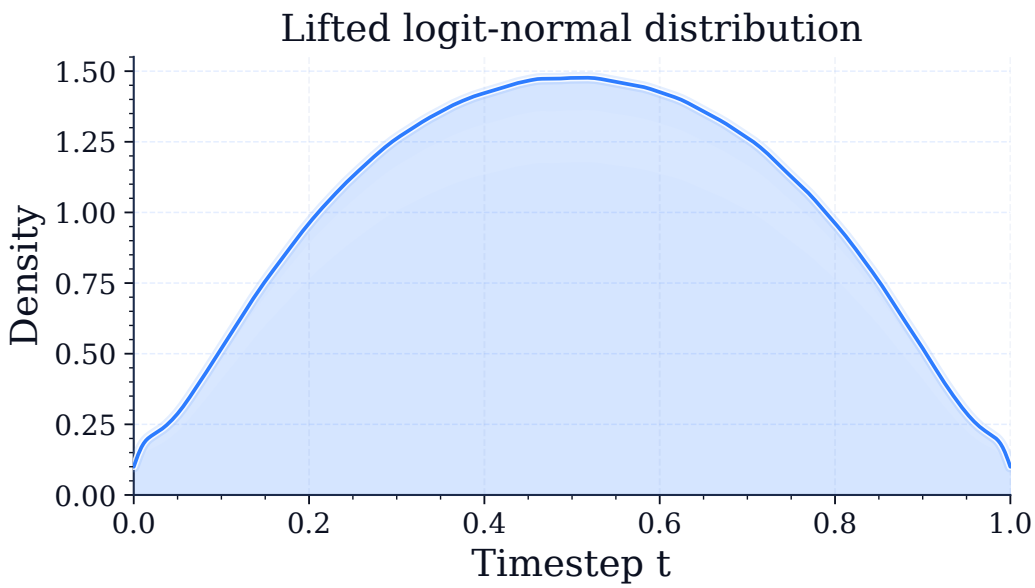

Figure 13: The density plot of the lifted logit-normal distribution ($\epsilon = 0.2$). Most of the mass is placed on values of t in the middle of the range $(0, 1)$ and a substantial amount near the endpoints.

H Lifted Logit-Normal Distribution

While training our geometry decoder with flow matching, we sampled the denoising timestep from the lifted logit-normal distribution, defined as

$$t = (1 - \mathrm{b}) \cdot t_{LN} + \mathrm{b} \cdot t_U$$
$$\mathrm{b} \sim \mathrm{Ber}(\epsilon),\ t_{LN} \sim \mathrm{LogitNorm}(0, 1),\ t_U \sim U[0, 1],$$

to prioritize the challenging denoising tasks from the midpoint timesteps (Esser et al., 2024) and ensure sufficient coverage of the edge timesteps (see Figure 13). We set $\epsilon = 0.1$.

I Inference Time Analysis

Unlike the generative baselines, our model does not simply sample new materials—it optimizes them in the latent space, with evolution strategies (ES, Appendix B) beforehand. This optimization phase, of course, incurs extra computational cost. In this section, we are going to discuss the resulting computational overhead. We note that, while doing so, we are not going to account for GPU-accelerated matrix multiplication algorithms. However, we are going to account for in-batch parallelism.

Recall that, at each latent-space optimization step, we sample N_{pert} perturbations ϵ of the optimized latent $\mathbf{z}$. Then, we predict the target property of antithetic samples with the predictive head, $f_\theta(\mathbf{z} \pm \sigma\epsilon)$, which is an MLP. Since the sampling and the evaluation step happen in parallel, the time induced in this step is $\mathcal{O}(N_{\text{layers}} d_{\text{model}}^2)$, where N_{layers} and d_{model} are the number of MLP layers and its hidden dimension, respectively. The obtained predictions are then ranked, which induces time cost of $\mathcal{O}(N_{\text{pert}} \log N_{\text{pert}})$ due to a sorting algorithm, such as Quicksort (Hoare, 1961). Then, the ranks are used to derive the ES gradient (Equation (8)) which, not requiring back-propagation, is a simple algebraic expression that can be omitted. Altogether, a single optimization step induces time cost of $\mathcal{O}(N_{\text{layers}} d_{\text{model}}^2 + N_{\text{pert}} \log N_{\text{pert}})$, and the total time of T-step latent-space optimization is

$$\mathrm{Time}(\mathrm{MBO}) = \mathcal{O}\big(T(N_{\text{layers}} d_{\text{model}}^2 + N_{\text{pert}} \log N_{\text{pert}})\big).$$

Note that this time does not depend on the number of materials optimized thanks to the batch parallelism. Additionally, since the model used in the latent space is a relatively small MLP, the resulting time overhead induced by the MBO phase is negligible in comparison to the time cost of

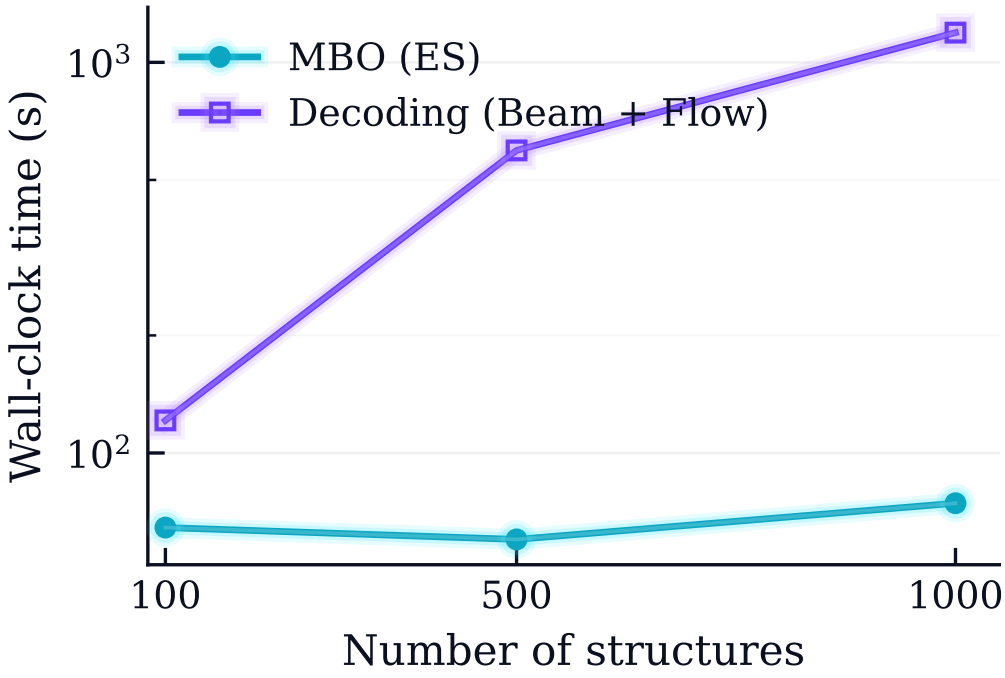

Figure 14: Wall clock time of material optimization with CliqueFlowmer. The optimization (MBO) step remains negligible, especially as the number of materials increases. The wall clock time is dominated by beam search but it remains linear in the number of structures.

the remaining phase consisting of generative modeling techniques. In particular, it stands in contrast with the beam search step (Appendix A.3) which, unlike the flow step, we do not parallelize. As a result, as the number of optimized materials increases, the beam search step becomes the most costly, although it remains at most linear in the number of structures. We note that transformer decoding and beam search can be optimized for efficiency as well (Yan et al., 2021; Frohner et al., 2022) but it is out of scope of this paper.

To demonstrate this, we conduct the following experiments. We encode and optimize, in the latent space, $N = \{100, 500, 1000\}$ materials and decode them back into the material form, without relaxation. We measure how much time, in seconds, the MBO and the decoding phases took in each experiment. For sample sizes 100, 500, and 1000, the MBO step took 64, 60, and 74 seconds, respectively, thus staying relatively constant. Meanwhile, the decoding step took 121, 595, and 1,192 seconds, respectively. See Figure 14 for visualization of the results. Using the largest sample as the approximation of the limit $N \to \infty$, we estimate that CliqueFlowmer allows for optimizing a single structure in 1.19 seconds on average.

Table 6: CliqueFlowmer hyperparameters.

Category	Parameter	Value	Description
Model	n_cliques	8	Number of latent cliques
	clique_dim	16	Dimensionality of each clique
	knot_dim	1	Overlap between adjacent cliques
	transformer_dim	256	Transformer hidden dimension
	n_blocks	4	Transformer layers
	n_heads	4	Attention heads
	n_registers	2	Register tokens
	mlp_dim	128	MLP hidden dimension
	n_mlp	2	MLP depth
	dropout_rate	0.1	Dropout probability
Training	gradient_steps	7×10^5	Number of gradient steps
	alpha_vae	10^{-4}	KL regularization limit
	alpha_mse	1	Prediction loss weight limit
	beta_mse	10^{-4}	Prediction loss weight init
	temp_atom	1	Atom weight in the loss
	temp_flow	16	Position weight in flow loss
	warmup	10^5	Linear warmup steps
	learning_rate	1.4×10^{-4}	Model learning rate
Latent-space Optimization	algorithm	ES	Algorithm used
	antithetic sampling	True	If antithetic sampling used
	n_pert	20	Number of perturbations
	pert_scale	0.05	Scale of perturbations
	learning_rate	3×10^{-4}	Latent optimization LR
	design_steps	2000	Latent optimization steps
	decay	0.4	Weight decay
Decoding	N_beam	10	Beam search width
	w_cfg	2	CFG (guidance) strength
	N_step	1000	Number of denoising steps

J Model and Optimization Hyperparameters

Table 6 summarizes the hyperparameters used throughout all experiments. Unless otherwise stated, these values are fixed across runs.

Additionally, for the band gap task, we defined the target property to be the formation energy-regularized band gap

$$f(\mathsf{M}) = \Delta_{\text{band}}(\mathsf{M}) + \lambda_{\text{reg}} \cdot \max\left(0, E_{\text{form}}(\mathsf{M}) - \tau_{\text{reg}}\right),$$

where we set $\lambda_{\text{reg}} = 20$ and $\tau_{\text{reg}} = -0.2$. The goal of adding the term $\lambda_{\text{reg}} \cdot \max\left(0, \mathcal{E}_{\text{form}}(\mathsf{M}) - \tau_{\text{reg}}\right)$ was to constrain the model's search space to low formation energy materials, as such tend to be more stable. Below this threshold, the objective would simply reduce to the band gap, and the penalty would only be induced for materials that exceed it.